Focus Section: Advances in Operational Response

The 15 January 2022, Eruption at Hunga Tonga–Hunga Ha'apai, Recorded by Multiparametric Geophysical Stations in Italy

OPEN ACCESS

Thomas Braun[*1,2], Claudio Cesaroni[2], Bellina Di Lieto[3], Marco Massa[4], Mariangela Sciotto[5], Alessandro Bonaccorso[5], Andrea Cannata[6], Luigi Carleo[3], Rosario Catania[7], Gilda Currenti[5], Gianfilippo De Astis[2], Marco Guerra[2], Alessandro Ippolito[2], Salvatore Roberto Maugeri[3], Massimo Orazi[3], Rosario Peluso[3], Andrea Luca Rizzo[4,8], Pierdomenico Romano[3], and Luca Spogli[2]

Abstract

On 15 January 2022, the main eruption of the Hunga volcano generated one of the most energetic atmospheric and geophysical disturbances ever instrumentally recorded. The explosion produced a global Lamb wave, tsunami waves across the Pacific Ocean, and ionospheric perturbations detectable worldwide. In Italy, the multiparametric monitoring networks operated by the Istituto Nazionale di Geofisica e Vulcanologia recorded the event through seismic, barometric, infrasonic, strain-meter, and Global Navigation Satellite System (GNSS) observations, providing a unique regional case study of long-range atmosphere–solid Earth coupling. In this work, we analyze observations from the Italian Seismic Network, volcano monitoring infrastructures at Etna, Stromboli, and Phlegraean Fields, meteorological and barometric stations, and the National GNSS Network. The eruption-generated atmospheric pressure wave was detected throughout Italy after propagating along the minor and major arcs of the globe, with an average velocity of approximately 310 m/s. Multiple passages of the Lamb wave were identified in barometric and infrasonic recordings over several days. Broadband seismic stations recorded not only teleseismic body and surface waves associated with the eruption, but also clear ground-coupled atmospheric waves at very low frequencies. Borehole strain meters unexpectedly showed highly correlated deformation signals induced by atmospheric pressure changes, highlighting strong seismoacoustic coupling. GNSS-derived total electron content measurements revealed traveling ionospheric disturbances linked to the upward propagation of atmospheric waves. The event shows that the GNSS network reliably detects the Lamb-wave-induced perturbations of an extreme, distant source within the same real-time infrastructure used for seismic and barometric monitoring. This confirms that total electron content can be produced and interpreted operationally alongside conventional parameters, supporting its use for closer, tsunamigenic sources as a complementary, globally distributed observable within a multiparametric early-warning framework. This study is the first of its kind in Italy, highlighting both the extraordinary nature of the volcanic eruption and the value of multiparameter data collected by instruments originally installed for other projects.

Cite this article as Braun, T., C. Cesaroni, B. Di Lieto, M. Massa, M. Sciotto, A. Bonaccorso, A. Cannata, L. Carleo, R. Catania, G. Currenti, *et al.* (2026). The 15 January 2022, Eruption at Hunga Tonga–Hunga Ha'apai, Recorded by Multiparametric Geophysical Stations in Italy, *Seismol. Res. Lett.* **XX**, 1–21, doi: 10.1785/0220260189.

1. Istituto Nazionale di Geofisica e Vulcanologia, Arezzo, Italy, https://orcid.org/0000-0003-1778-1328 (TB); 2. Istituto Nazionale di Geofisica e Vulcanologia, Rome, Italy, https://orcid.org/0000-0003-2268-4389 (CC); https://orcid.org/0000-0003-2057-1276 (GDA); https://orcid.org/0000-0001-9993-2366 (MG); https://orcid.org/0000-0003-3823-127X (AI); https://orcid.org/0000-0003-2310-0306 (LS); 3. Istituto Nazionale di Geofisica e Vulcanologia, Naples, Italy, https://orcid.org/0000-0001-8093-3051 (BDL); https://orcid.org/0000-0001-7533-1400 (LC); https://orcid.org/0000-0003-4330-3434 (SRM); https://orcid.org/0000-0003-2772-2989 (MO); https://orcid.org/0000-0001-6276-5832 (RP); https://orcid.org/0000-0002-2380-0567 (PR); 4. Istituto Nazionale di Geofisica e Vulcanologia, Milan, Italy, https://orcid.org/0000-0003-2225-3781 (ALR); 5. Istituto Nazionale di Geofisica e Vulcanologia, Catania, Italy, https://orcid.org/0000-0001-8711-1392 (MS); https://orcid.org/0000-0002-4770-6006 (AB); https://orcid.org/0000-0001-8650-5613 (GC); 6. Department Biologic, Geologic, Environment Sciences, University of Catania, Catania, Italy, https://orcid.org/0000-0002-0028-5822 (AC); 7. STMicroelectronics s.r.l., Agrate Brianza, Italy, https://orcid.org/0009-0003-4616-342X (RC); 8. Department of Earth and Environmental Sciences (DISAT), University of Milano-Bicocca, Milan, Italy

*Corresponding author: thomas.braun@ingv.it

Copyright © 2026. The Authors. This is an open access article distributed under the terms of the CC-BY license, which permits unrestricted use, distribution, and reproduction in any medium, provided the original work is properly cited.

Downloaded from pubs.geoscienceworld.org/ssa/srl/article-pdf/doi/10.1785/0220260189/8448745/srl-2026189.1.pdf by Universidad de Buenos Aires user on 27 November 2026

Introduction

The Hunga Tonga–Hunga Ha'apai (HTHH) volcano is located along the Kermadec–Tonga volcanic arc (KTva), which is intraoceanic and originated to the west-northwest of the Tonga Trench, due to the westward subduction of the Pacific Plate under the Australian Plate. Here, we observe the fastest converging boundary in the world (24 cm/yr), which decreases southward to 6 cm/yr (Smith and Price, 2006). For geodynamics, it has become a test case for defining and explaining models for the tectonic and magmatic evolution of intraoceanic subduction systems. Together with the volcanic island arc, there is a seafloor ridge that extends from New Zealand to Tonga, having one of the highest numbers of seamounts in the world (De Ronde *et al.*, 2007).

The main eruption of 15 January 2022, occurred at around 04:15 UTC (+ 13 hr local time) and lasted only about 10 min, but was so violent that atmospheric pressure waves (Lamb waves) surrounded the globe several times, and Pacific islands, as well as coastal areas, recorded a tsunami, with damaging effects on Tonga Island and being recorded also in Japan, South America, and Australia. The Lamb wave-driven perturbations were also detected over the central Mediterranean by Matoza *et al.* (2022) and Madonia *et al.* (2023), who documented their propagation across multiple atmospheric layers, from tropospheric pressure waves recorded by barometric and infrasound sensors on Italian volcanoes to ionospheric total electron content (TEC) enhancements retrieved from Global Navigation Satellite System (GNSS) and ionosonde data.

Matoza *et al.* (2022) and Kraft *et al.* (2023) (among the others) reported that the climactic explosion of the HTHH generated a low-frequency (~4 mHz) atmospheric pressure perturbation (Lamb wave, Lamb, 1881) comparable in energy and atmospheric impact with the famous 1883 Krakatau eruption. The pressure wave circled the Earth four times directly (plus three times via its antipodal point), remaining detectable on surface microbarographs and weather sensors worldwide for over 6 days. Energy propagating into the upper atmosphere triggered noticeable disturbances in the Earth's ionosphere. Audible booms were heard at extreme distances, notably 10,000 km away in Alaska as distinct booms, or in Europe, probably generated by the intense volcanic lightning activity (Kraft *et al.*, 2023). Seismometers around the globe recorded both solid-Earth seismic waves and acoustic waves that coupled into the ground as the atmospheric pressure pulse passed overhead (Anthony *et al.*, 2022; Matoza *et al.*, 2022; Macpherson *et al.*, 2025; Scamfer *et al.*, 2026). The atmospheric Lamb wave traveled at around 315 m/s, faster than typical open-ocean tsunami waves, transferring energy into the ocean via air–sea coupling, explaining why tsunami waves arrived significantly earlier at distant coastlines than standard ocean-gravity tsunami models predicted.

The diameter of the eruption cloud was estimated to be 500 km (Venzke, 2022; Van Eaton *et al.*, 2023), reaching a height of 30 km (National Oceanic and Atmospheric Administration [NOAA]; Taha *et al.*, 2022) and more than 50 km (Proud *et al.*, 2022) according to satellite observations and subsequent analyses. The explosion energy was estimated between 4 and 18 Mt of TNT (Purkis *et al.*, 2023), which corresponds to at least 500 times stronger than the bomb dropped on Hiroshima in 1945 (Garvin, 2022).

Studies of ongoing submarine explosive eruptions are relatively rare. Observations are limited to those shallow seamounts where the eruptions reached the surface, showing changes in the color of the overlying seawater or floating pumice, or triggering Surtseyan activity (Fiske *et al.*, 1998; Baker *et al.*, 2002; Carracedo *et al.*, 2012; Perttu *et al.*, 2020).

The eruptive activity that occurred in December 2021–January 2022 and the sequence of related natural phenomena represented an unprecedented opportunity to investigate a unique geophysical dataset and a variety of volcanologic and atmospheric processes involving hydrothermal fluids, magmatic gas discharge, magma fragmentation, tephra dispersion, acoustic–gravity waves, and ionospheric perturbations. The HTHH eruption rapidly became one of the most comprehensively monitored volcanic crises in modern geophysics because it was simultaneously detected by seismic, barometric, infrasonic, GNSS, and satellite systems distributed worldwide.

In recent years, one of the main efforts of the Istituto Nazionale di Geofisica e Vulcanologia (INGV) has been the development and integration of real-time sources and platforms capable of combining seismic, geodetic, infrasonic, ionospheric, and meteorological observations into multiparametric monitoring frameworks. These infrastructures are designed not only for volcano and earthquake surveillance, but also for supporting early warning applications and rapid science communication and delivery to decision makers during complex geophysical crises. The HTHH eruption provided a unique large-scale experiment to evaluate the performance of these monitoring systems and their capability to detect atmospheric and solid Earth coupling phenomena at local, regional, and global scales.

The observations collected by the Italian monitoring networks also represent important regional case studies for understanding how extreme volcanic events can be detected thousands of kilometers away from the source through different physical observables. In particular, the simultaneous recording of Lamb waves, pressure perturbations, seismic ground coupling, and ionospheric disturbances demonstrates the importance of integrating heterogeneous monitoring systems operating in real time. Such integrated approaches are becoming increasingly important for improving hazard assessment strategies and strengthening international cooperation in geophysical monitoring.

Downloaded from pubs.geoscienceworld.org/ssa/srl/article-pdf/doi/10.1785/0220260189/8448745/srl-2026189.1.pdf by Universidad de Buenos Aires user on 27 November 2026

In this article, we describe the multiparametric observations recorded by the different INGV monitoring networks during and after the HTHH eruption. We analyze seismic, infrasound, barometric, strain-meter, and GNSS measurements to characterize the propagation of atmospheric and seismic disturbances associated with the eruption and to investigate their signatures across Italy and the central Mediterranean region.

Our results demonstrate the effectiveness of integrated, real-time sources and platforms in detecting and characterizing extreme geophysical events across local, regional, and global scales. Once processing times are reduced to near-real time, these data analysis products have the potential to significantly support early warning systems, emergency responses, and rapid scientific communication.

Geological Setting

Recent phreatomagmatic activity at HTHH was observed in 2009 and 2014/2015, giving rise to typical Surtseyan eruptions (interaction of magma with the shallow water and explosive disruption of rapidly cooled magma). In March–April 2009, this activity occurred from two vents along the western shore of Hunga Ha'apai and was characterized by repeated explosions with ash and steam plumes some kilometers high and base surge dispersion, estimated to be volcanic explosivity index (VEI) = 2 (Vaughan and Webley, 2010). Scoriae, cinder, and tuff deposits accumulated in such a huge amount that the two islets were interconnected. A detailed report of the 2014/2015 eruption can be read on the Global Volcanism Program website. Here we think it is enough to report that the Surtseyan activity started on 19 December 2014, with tephra jets several hundred m high, progressively adding land between the two islets, creating the merged HTHH island.

After 7 yr of quiescence, HTHH woke up on 19 December 2021 (20:30 UTC), generating an eruptive cloud up to a height of 16–18 km (Korea's GeoKompsat weather satellite; see Data and Resources; Japan Meteorological Agency Himawari-8 data). The following two weeks were characterized again by "Surtseyan" activity, growing up a cinder cone northeast (NE) of the 2014–2015 deposits, and a variable and pulsating eruptive column on 14 January 2022, one day before the main event, a massive eruption plume rising above HTHH was captured by the GOES-17 satellite (NOAA) at 06:40. The ash cloud reached a height of 20 km and expanded radially at the top to 240–260 km in diameter, being so strong that the interconnecting part of both islands dropped again below sea level, significantly changing the islets morphology.

Data and Instrumentation

This section describes the instrumentation and networks running at INGV that recorded signals associated with the eruption of HTHH:

Seismic stations (IV): The Istituto Nazionale di Geofisica e Vulcanologia (INGV) operates a seismic monitoring network RSN (INGV, 2006), installed throughout the national territory (Federation of Digital Seismic Networks [FDSN] network code IV, see Data and Resources) and the Mediterranean Seismic Network–MedNet (Pondrelli *et al.*, 2019) (FDSN network code MN, see Data and Resources). MiniSEED data streams are transmitted in real time to the monitoring center in Rome (and partially to Naples and Catania), where the location and magnitude of the recorded seismic events are calculated H24/7 (Margheriti *et al.*, 2021). INGV is a primary node of the European Integrated Data Archive (see Data and Resources) for archiving and distributing weak and strong motion and motion seismic recordings (Massa *et al.*, 2014; Luzi *et al.*, 2016; Michelini *et al.*, 2016). Today, the RSN consists of about 400 seismometer stations, 60% equipped with broadband sensors (20–360 s); about 70% of the RSN stations are connected to an accelerometer.

The yellow triangles in the map inset in Figure 1 depict the seismic stations (IV) operating on Vulcano and Lipari islands (see Figure 2 and the Seismological observations section). The yellow inverted triangles in Figure 1 show the geographical position of the seismic stations used in this study (see the Seismic Signatures section); and red and blue lines indicate some of the minor (red) and major (blue) arcs.

Barometric stations (AM): The Meteorological Service (IAFMS) of the Italian Air Force (IAF) manages an extensive network of observation stations, which monitor barometric parameters (atmospheric pressure, white squares in Fig. 1) and other fundamental climate data across the entire national territory. These stations are essential for flight safety and for the formulation of official weather forecasts in Italy (circles in Fig. 1).

Barometric and infrasound stations (IV): INGV operates barometric (see the Barometric observations section) and infrasound stations (see the Infrasound observations section) for the monitoring of the active volcanoes. For the present study, we used the instruments installed on Mt. Etna, Stromboli, and Phlegraean Fields (red volcano symbols in Fig. 1).

The technical characteristics of the sensors used in this study are:

- A barometric pressure transducer, Setra model 278, in a range of 800–1100 hPa/mb, acquires data at a sampling rate of 1 Hz. The barometer is installed in the dilatometer stations that measure volumetric strain variations using a Sacks–Evertson strain meter;
- GRAS 40 AN microphone with a sensitivity of 50 mV/Pa. The frequency response of the instrument is flat in the range between 1 Hz and 10 kHz (±1 dB; ±2 dB from 0.5 Hz to 20 kHz). The infrasonic signal is acquired at a sampling rate of 50 Hz.

Weather station (ERO-INGV): Etna Radio Observatory (ERO) and INGV-OE operate weather stations near the VLF-band and microwave stations. The data presented in Figure 3 were recorded by the reference station installed in the city center

Downloaded from pubs.geoscienceworld.org/ssa/srl/article-pdf/doi/10.1785/0220260189/8448745/srl-2026189.1.pdf by Universidad de Buenos Aires user on 27 November 2026

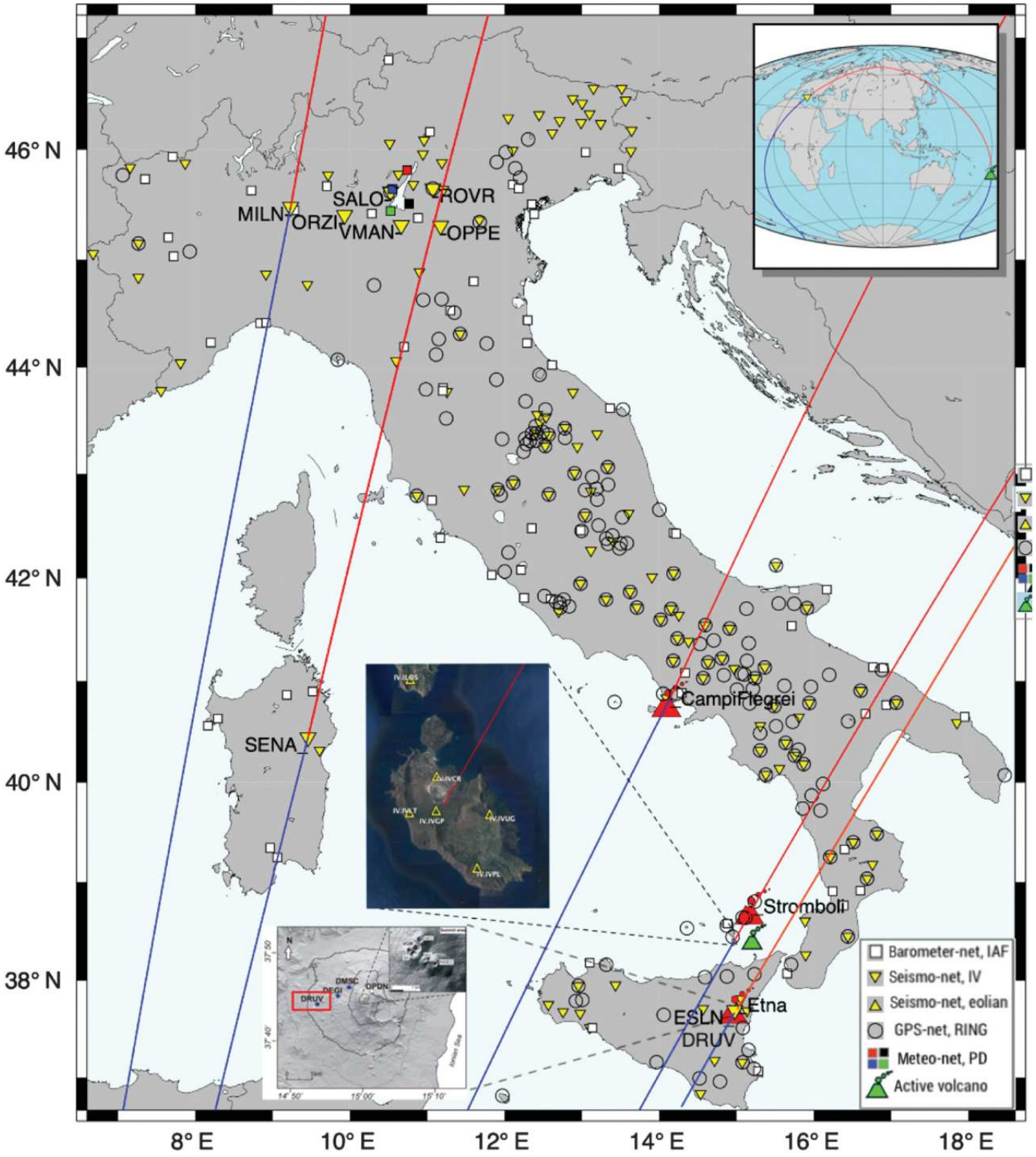

Figure 1. Overview of the stations used in this study. The squares indicate barometric stations of the Italian Air Force (white) and the PD-meteo-net (black, red, green, and blue, according to colors in Fig. 4); the volcano symbol indicates active volcanoes equipped with infrasound and barometric stations; the triangles indicate seismic stations installed at Vulcano and Lipari; the inverted triangles indicate seismic stations of the RSN. The circles indicate stations of the RING network. Great circles between Italian stations and HTHH are plotted for the short and long distances, by red and blue lines, respectively. The insets show the minor (red) and major arcs (blue) on a global scale (upper right) and a zoom-in of the seismic stations installed on the Eolian Islands. GPS, Global Positioning System.

Downloaded from pubs.geoscienceworld.org/ssa/srl/article-pdf/doi/10.1785/0220260189/8448745/srl-2026189.1.pdf by Universidad de Buenos Aires user on 27 November 2026

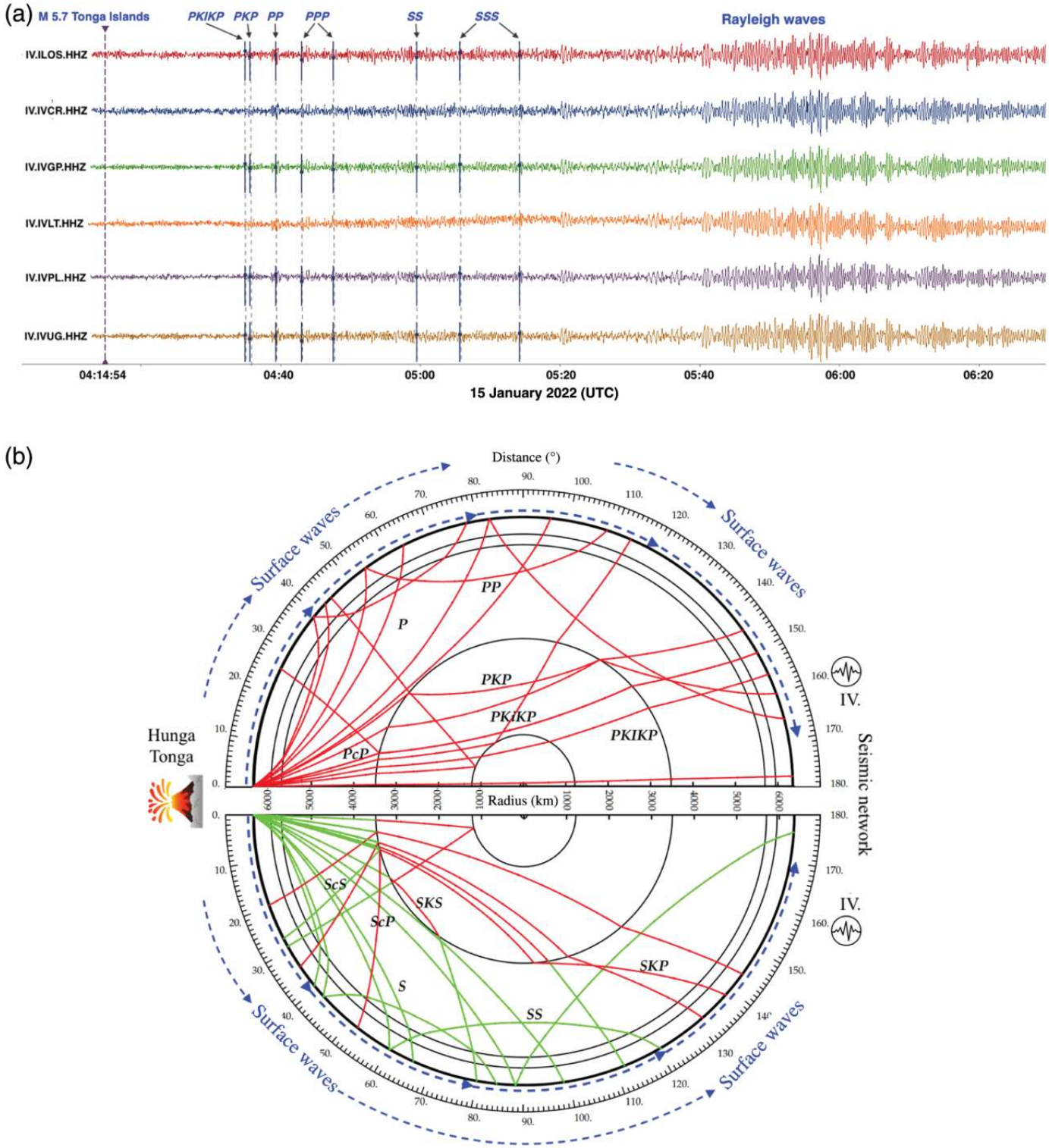

Figure 2. (a) HHZ-traces recorded at stations installed on the Eolian Islands (yellow triangles in Fig. 1), located at an epicentral distance of ~160° from HTHH. (b) Ray paths of *P* and *S* phases (modified after Kennett *et al.*, 1995).

of Catania 37.52571° N, 15.09033° E and are sampled every 5 min. The meteorological station is of type Ecowitt GW1000, equipped with an Hoperf HP203N pressure sensor.

Multiparameter network in northern Italy (PDnet, ZO): PDnet (FDSN code ZO, see Data and Resources) is a real-time multiparameter network installed in 2021 around the seismic area of Garda Lake (northern Italy, Massa *et al.*, 2021). The network consists of eight stations characterized by

Downloaded from pubs.geoscienceworld.org/ssa/srl/article-pdf/doi/10.1785/0220260189/8448745/srl-2026189.1.pdf by Universidad de Buenos Aires user on 27 November 2026

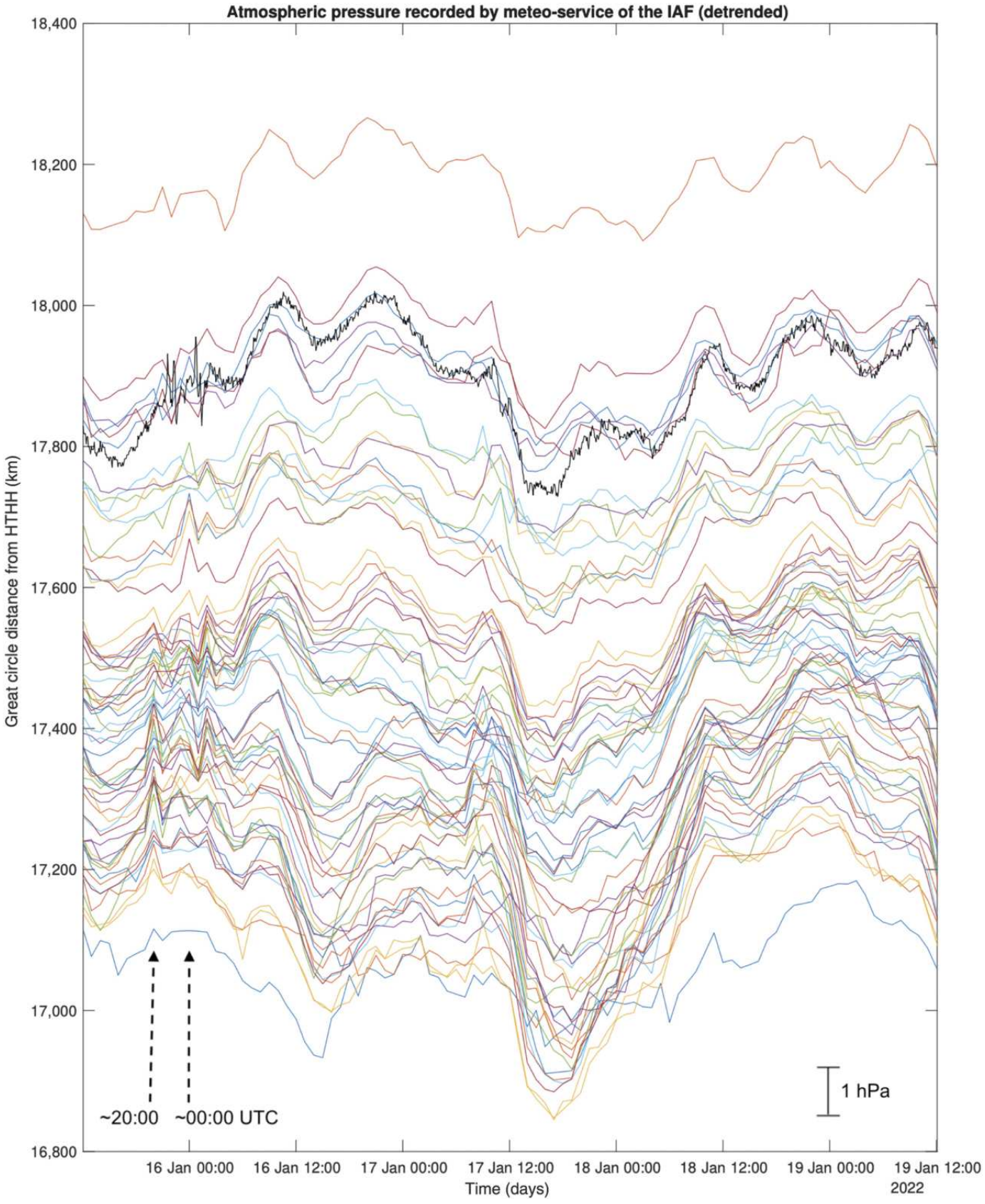

Figure 3. Detrended temporal variations of the barometric pressure recorded by the stations operated by the Meteorological Center of the Italian Air Force (IAF; white circles in Fig. 1). The pressure traces are ordered according to the epicentral distance (in black: the meteorological station Catania, operated by Istituto Nazionale di Geofisica e Vulcanologia, sampling interval 5 min).

Downloaded from pubs.geoscienceworld.org/ssa/srl/article-pdf/doi/10.1785/0220260189/8448745/srl-2026189.1.pdf by Universidad de Buenos Aires user on 27 November 2026

TABLE 1
Weather Stations of the PD-Network

Station	Locality	Latitude	Longitude	Altitude (m.a.s.l.)
PDN1	Bardolino	45.509860	10.764510	137
PDN4	Desenzano del Garda	45.442860	10.525600	157
PDN6	Gardone Riviera (Gere)	45.640790	10.550240	398
PDN3	Tremosine (Valle di Bondo)	45.813220	10.737430	699

short-period 5 s seismometers and accelerometers coupled with groundwater level, temperature, and water conductivity Van Essen CTD divers installed in selected wells. The divers are connected to Eijkelkamp data transmitters equipped with internal barometric and temperature sensors that make a measurement every hour to compensate for the barometric pressure of the divers. The network consists moreover of Davis Vantage Vue wireless weather stations equipped with a sensor array for monitoring essential environmental parameters (rain, wind speed and direction, atmospheric pressure, humidity, and temperature). The stations selected for this study are reported in Table 1 below and carried out measurements every 30 min. The barometric sensors installed in the weather stations recorded a variation due to the atmospheric pressure wave generated by the volcanic explosion of HTHH that is described in the following sections. Because of the lower sampling frequency (1 per hour) of the barometric sensors installed in the divers data transmitter, we will focus on the data provided by the weather stations only.

Rete Integrata Nazionale GNSS: Inside the frame of the RSN, the INGV operates the Rete Integrata Nazionale GNSS (RING, see Data and Resources): a collection of more than 200 geodetic stations scattered across the Italian territory. Thanks to the stations being placed in the free field and to the choke-ring antenna, the stations are characterized by low levels of multipath, making the data suitable for ionospheric studies. The data used are Global Positioning System carrier phase observables on L1 and L2 frequencies, clear acquisition, CA, code observables on L1, and Y-code observables on L2 that are broadcast at a 30 s rate through Networked Transport of Radio Technical Commission for Maritime Services (RTCM) via Internet Protocol (NTRIP) and saved in RINEX format. Figure 1 shows the spatial distribution of the station used for this study.

Observations

Seismological observations

The eruption of the volcano HTHH on 15 January 2022 04:14:54 UTC was analyzed using a globally distributed collection of stations. The magnitude was estimated as M_w 5.7 (Matoza *et al.*, 2022). As an example for the Italian Seismic Network IV, Figure 2a shows the HHZ traces recorded at stations installed on the Eolian Islands (Fig. 1), located at an epicentral distance of ∼160° from HTHH. The radiated seismic energy was strong enough to record core phases (*PKIKP* and *PKP*), surface reflection of mantle phases (*PP* and *SS*), as well as Rayleigh waves (Fig. 2b).

Barometric observations

Barometric data from IAFMS: Figure 3 shows the temporal variation of the absolute barometric pressure (hPa), sampled once an hour, for the single stations of the IAFMS-network (circles in Fig. 1). Data have been kindly provided for the time window between 15 January 2022 at 00:00 UTC and 20 January 2022 at 23:00 UTC.

Barometric stations of the PD-net: The barometric sensors installed at the PD-net weather stations around the Lake Garda seismic area (northern Italy, Ferrari *et al.*, 2024) recorded a clear atmospheric pressure perturbation associated with the Lamb wave generated by the Hunga eruption. A coherent positive pressure excursion was recorded at Desenzano, Bardolino, Gere, and Valle Bondo between 19:30 and 20:00 UTC on 15 January 2022, corresponding to the first arrival propagating along the shorter great-circle path and approaching the area from NE (Fig. 4).

The observed pressure excursion was of the order of 1 hPa; however, the actual pressure extrema may have occurred between consecutive samples, and therefore the measured amplitude should be regarded as an approximate value and may underestimate the true peak-to-peak perturbation. The great-circle distance between Hunga and the Lake Garda area is approximately 17.2×10^3 km. Considering an eruption time of about 04:15 UTC and the first arrival between 19:30 and 20:00 UTC, the resulting average propagation velocity is approximately 310 m/s, consistent with the propagation velocity of the Lamb wave observed at global scale.

Following the first arrival, the PDnet records show an additional pressure perturbation around 23:00 UTC on 15 January 2022 (Fig. 4). A comparable intermediate-to-long-range atmospheric pressure pulse has been reported in previous observations of the Hunga event and discussed in relation to the complex propagation of the atmospheric disturbance (Madonia *et al.*, 2023). This feature should therefore be distinguished from the subsequent arrival of the Lamb wave propagating along the opposite great-circle path. The latter, approaching the Lake Garda area from southwest (SW), is expected and observed around 01:00 UTC on 16 January 2022 (Fig. 4). In the PDnet records, this second arrival is less sharply defined than the first one and is expressed as a broader pressure perturbation extending approximately until 02:00 UTC. Because of the 30-min sampling interval, the timing of both arrivals can only be constrained within 30-min

Downloaded from pubs.geoscienceworld.org/ssa/srl/article-pdf/doi/10.1785/0220260189/8448745/srl-2026189.1.pdf by Universidad de Buenos Aires user on 27 November 2026

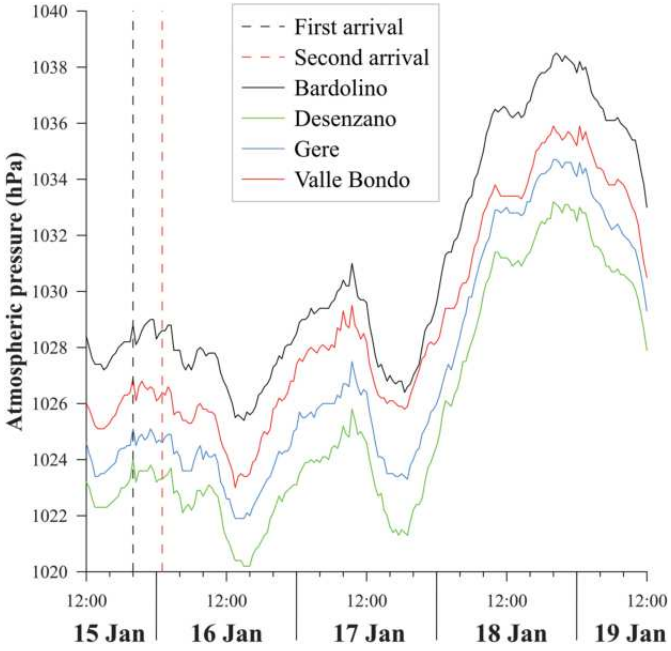

Figure 4. Temporal variations of atmospheric pressure recorded by the PDnet weather stations installed around Lake Garda between 15 and 19 January 2022. Pressure traces are vertically ordered according to their absolute barometric pressure. The first dashed vertical line indicates the first Lamb-wave arrival, propagating along the shorter great-circle path and approaching the area from the northeast, recorded between 19:30 and 20:00 UTC on 15 January 2022. A further pressure perturbation is visible around 23:00 UTC. The second dashed vertical line indicates the second Lamb-wave arrival, propagating along the opposite great-circle path and approaching from the southwest, at approximately 01:00 UTC on 16 January 2022; the associated pressure disturbance appears to extend until approximately 02:00 UTC.

windows (corresponding nominally to ± 15 min when an arrival time is assigned to the nearest sample). Likewise, the amplitudes reported from the PDnet records represent sampled values rather than necessarily the true pressure extrema, which may occur between consecutive measurements.

Global–regional–local: Figure 5a shows the barometric signals recorded by 20 stations located worldwide at distances ranging from ~750 to ~20,000 km from HTHH, available from the Incorporated Research Institutions for Seismology Data Management Center. As previously highlighted by other authors, for example, Matoza *et al.* (2022), Yuen *et al.* (2022), and Vergoz *et al.* (2022), such signals clearly show the propagation of the Lamb wave produced by the HTHH explosion with an approximate velocity of 310 m/s.

These values were obtained by calculating the travel time using the origin time of the associated seismic event (15 January 2022 04:14:45 UTC, see Data and Resources) and the arrival time at the Etna station (15 January 2022 20:10:00 UTC), dividing by the great-circle distance.

The Lamb wave is mainly characterized by a long period (> 2000 s; Vergoz *et al.*, 2022) and was recorded several times by the barometers due to several minor-arc and major-arc wave passages. Signals recorded by denser barometer networks in Italy at both regional and local scales show features in agreement with the features identified at global scales. Indeed, barometric stations installed at Phlegraean Fields (CF–Campi Flegrei), Stromboli, and Etna in the dilatometer stations recorded the pressure wave generated by the volcanic explosion of HTHH. Its amplitude exceeds the signal-to-noise ratio (SNR) of the background level (Fig. 5b). The first arrival, coming from NE, is recorded at CF station at 19:57 UTC, at Stromboli at 20:09 UTC, and at Etna at 20:13. The barometric sensors installed in the dilatometer stations at Etna (Fig. 5c) show a maximum time delay of about 20 s in the pressure signals between the more distant stations (DPDN and DRUV). The observed time delays among the stations agree with the apparent velocity value expected for a pressure wave coming from NE. After traveling along the minor arc, the second arrival from SW is recorded at about 03:15 hr at Etna, at 03:28 hr at Stromboli and 03:53 hr at CF after the first one, in agreement with the global propagation velocity of 310 m/s. The explosion is so energetic that it has been possible to record also the second and third tours around the globe of the blast wave (about 34 and 72 hr later, respectively), before its complete attenuation.

Atmospheric pressure variations induce deformation in the Earth's crust that is instantaneously recorded by borehole strain meters with a sensor response strongly dependent on the site. In the conventional analysis of strain data, such variations are generally regarded as spurious signals. In fact, investigating processes that originate and occur within the Earth's crust and lithosphere requires estimating the atmospheric contribution to crustal and lithospheric deformation and removing it from the observed data. This procedure made it possible to reliably identify individual spheroidal modes of the Earth's free oscillations that were masked by atmospheric variations in the original measurements. However, in a few cases, these variations can be the main signals that give us important information: they may represent the primary signals capable of providing valuable information about the ongoing dynamics.

The pressure wave generated by the volcanic explosion of HTHH was strong enough to induce significant strain variations up to tens of nano strain at the dilatometer stations (Fig. 6). The cross-correlation between the pressure and strain signals was 0.98 at CF and Etna and 0.81 at Stromboli, denoting a constant and in-phase response of the ground to low-frequency barometric pressure changes. This observation about strain–infrasound mechanical coupling evidences the potential of strain meters for seismoacoustic analysis and emphasizes the use of those recordings combined with seismic, geodetic, and infrasonic datasets to help in better understanding the coupling between the Earth's crust and the atmosphere.

Downloaded from pubs.geoscienceworld.org/ssa/srl/article-pdf/doi/10.1785/0220260189/8448745/srl-2026189.1.pdf by Universidad de Buenos Aires user on 27 November 2026

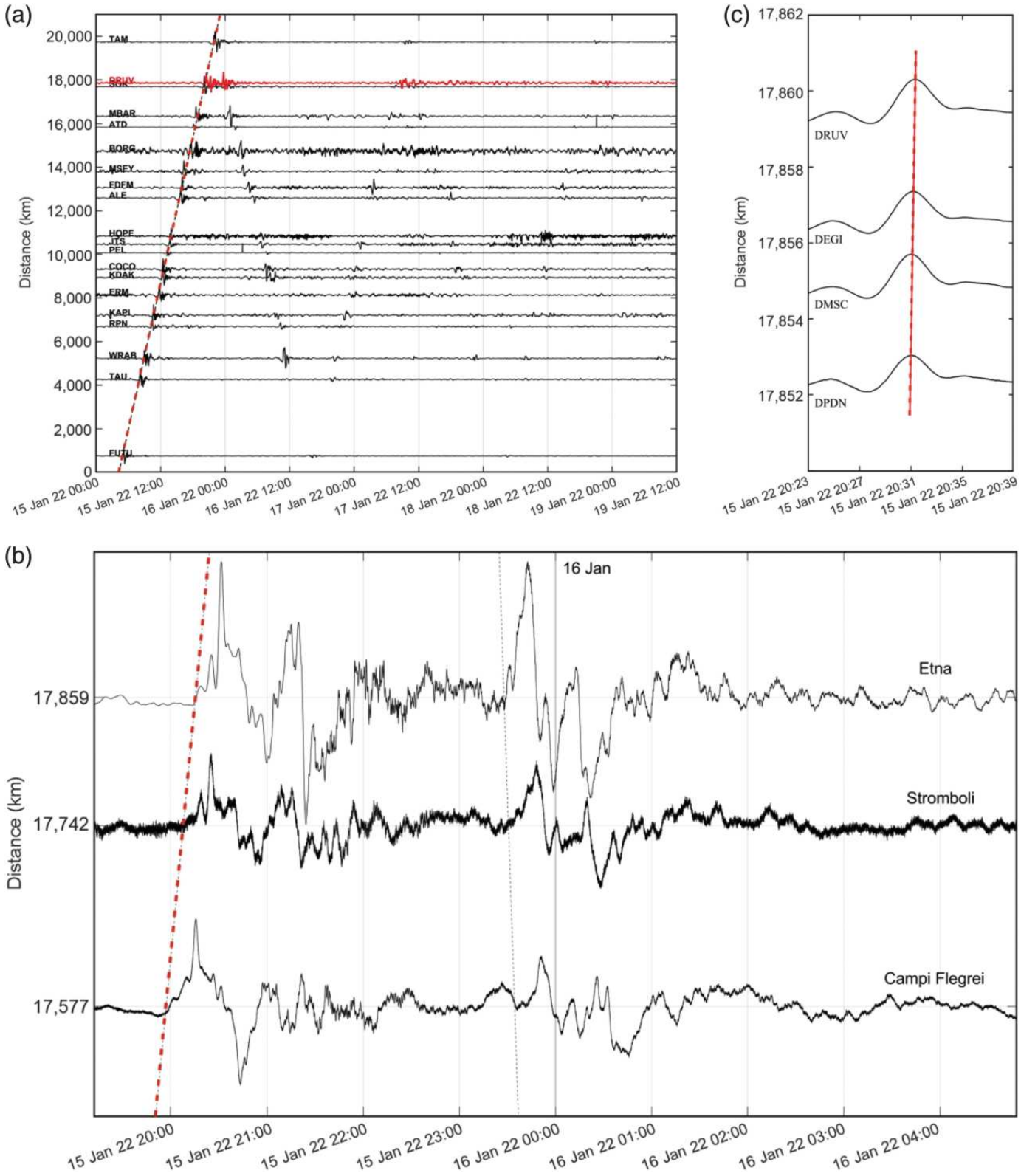

Figure 5. Time–distance plot of pressure variations recorded by INGV–OV and INGV–OE barometric stations at (a) global, (b) regional (Yuen *et al.*, 2022), and (c) local scale. (a) Pressure data recorded at the DRUV barometer (red trace), installed on Etna Volcano, plotted together with pressure data from barometers installed all over the globe (black traces; data from Incorporated Research Institutions for Seismology Data Management System, see Data and Resources), aggregated by radial distance and filtered by a four-pole Butterworth high-pass filter with a cutoff frequency of $0.7 \cdot 10^{-4}$ Hz. The red dashed line was obtained by assuming a velocity of 0.31 km/s. (b) Pressure data recorded on Etna (DRUV), Stromboli (SVO) and Quarto (CQUE) stations filtered above $0.9 \cdot 10^{-4}$ Hz (3 hr period).

Downloaded from pubs.geoscienceworld.org/ssa/srl/article-pdf/doi/10.1785/0220260189/8448745/srl-2026189.1.pdf by Universidad de Buenos Aires user on 27 November 2026

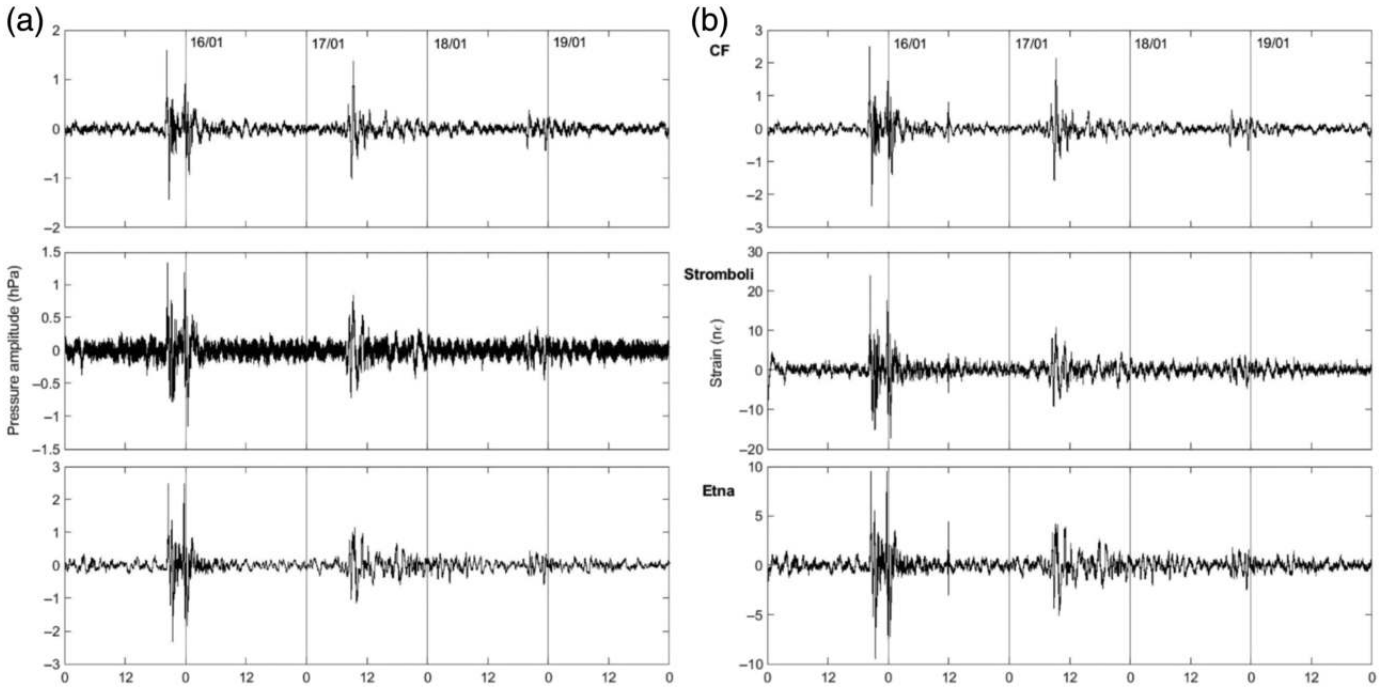

Figure 6. (a) Barometric pressure and (b) pressure-induced signal in the strain meter. High correlation coefficients are found at CF (0.98), Etna (0.98), and Stromboli (0.81).

Infrasound observations

To identify and characterize infrasonic waves generated by the HTHH eruption, we analyzed the amplitude envelope (root mean square [RMS] estimated using 10 min long windows overlapped by 30 s) and the spectral content (represented by means of spectrograms averaged over consecutive 10 min windows, with a 60 s Welch window and 50% overlap) of signals recorded by stations of the Infrasound Permanent Network installed on Mount Etna (INGV-OE).

The Hunga eruption generated a broad spectrum of atmospheric waves, including Lamb waves, acoustic gravity waves, and infrasonic waves, as already published by, for example, Matoza *et al.* (2022), Podglajen *et al.* (2022), and Vergoz *et al.* (2022). In particular, the infrasonic component extended over a broad frequency range, from approximately 0.01 Hz to several Hertz (Matoza *et al.*, 2022; Vergoz *et al.*, 2022), although the long-range infrasonic wave packets were predominantly observed at frequencies of a few tens of millihertz (mHz) (Podglajen *et al.*, 2022; Vergoz *et al.*, 2022). Their identification at Mt. Etna may therefore be challenging because of wind-induced noise, the possible presence of local volcano-generated infrasonic signals, and the frequency response of the instrument (see the Data Instrumentation section).

Nevertheless, RMS amplitude envelope and relative spectrograms show a clear increase in infrasonic amplitude observed on 15 January 2022, at several of the lower-elevation stations (EMFS, EMFO, EMNR, and ESLN), with similar spectral content below 2 Hz, whereas no comparable increase is evident at ESVO station and at the summit stations (ECPN, EPDN, and EPLC) (Fig. 7a,b). This difference may be related to the aforementioned different noise conditions affecting the stations, which may reduce the SNR of the transient associated with the Hunga eruption. The wavefronts were recorded again in the following days, after having circumnavigated the Earth's atmosphere; the second one is visible at around 10:00 UTC on 17 January 2022, as a weaker increase in RMS amplitude at ESLN station, while the third is not identifiable (Fig. 7a).

Madonia *et al.* (2023) reported the arrival of the HTHH-Lamb wave in the barometric record at Mount Etna and reported a delay of approximately 1 hr before the arrival of a higher-frequency signal recorded by an infrasonic station, interpreted as a separate component of the atmospheric disturbance. A closer inspection of the infrasound signal between 18:00 UTC on 15 January and 08:00 UTC on 16 January 2022 reveals several distinct amplitude increases, with the first and most energetic ones occurring at approximately 21:10, 22:55, and 00:42 UTC (Fig. 7c,e). The spectrogram, calculated using 4096-sample (81.92 s) windows with 75% overlap, shows two persistent spectral lines throughout the analyzed period, at approximately 0.3 and 1 Hz (clearly identifiable even at other stations, Fig. 7b,d), which are likely related to local volcanic activity. Superimposed on these persistent signals, additional energy attributable to wavefronts generated by the Hunga eruption is observed. Most of this energy is concentrated below 2 Hz and appears as an infrasonic tremor in the helicorder (Fig. 7d,e).

The complex temporal structure of the signal can be attributed to a combination of source and propagation effects. First, the HTHH eruption involved a complex sequence of explosive

Downloaded from pubs.geoscienceworld.org/ssa/srl/article-pdf/doi/10.1785/0220260189/8448745/srl-2026189.1.pdf by Universidad de Buenos Aires user on 27 November 2026

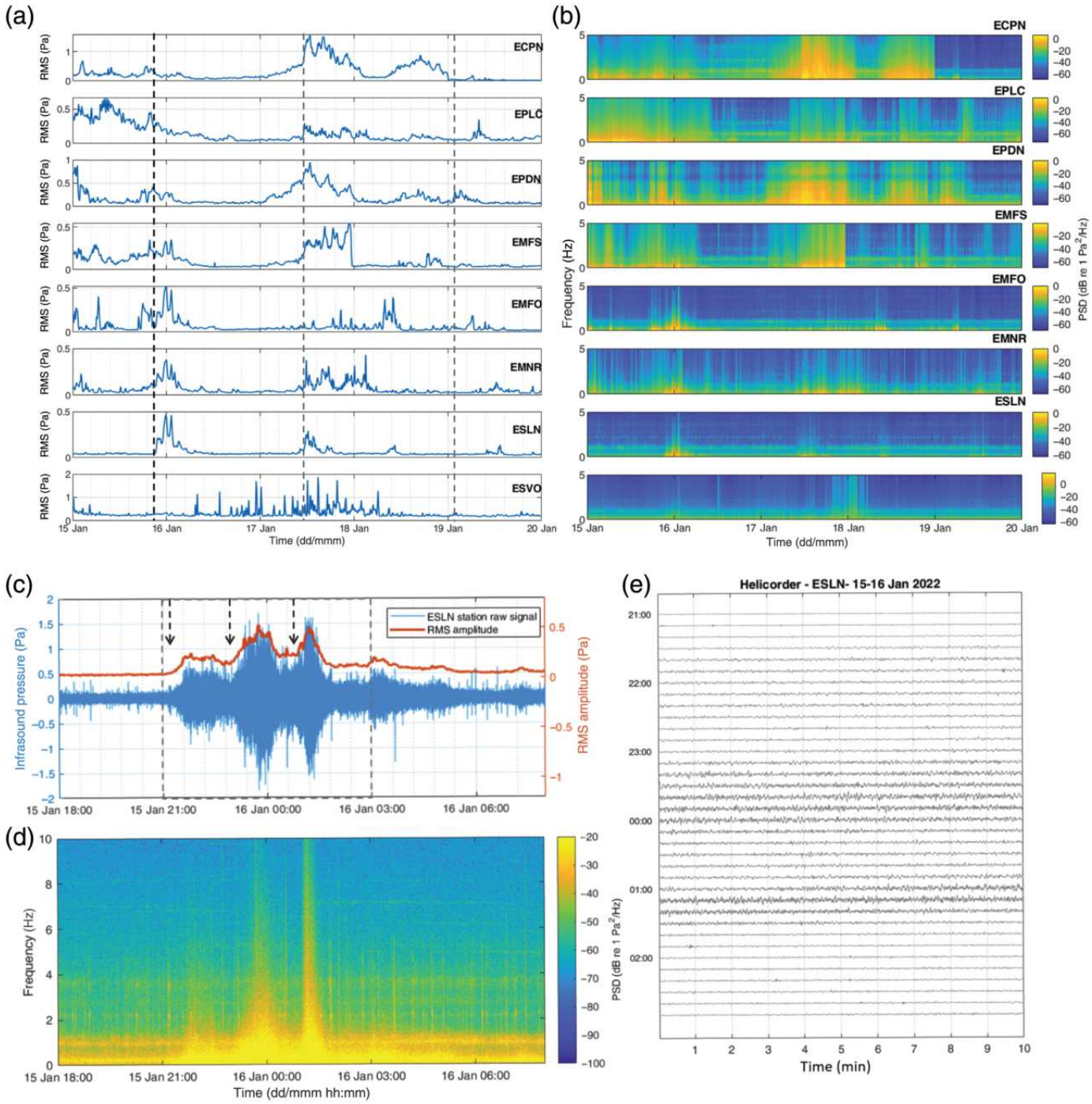

Figure 7. (a) Temporal evolution of the root mean square (RMS) amplitude of the raw infrasonic signals recorded by the INGV-Infrasonic Permanent Network from 15 to 19 January 2022. Each subplot corresponds to an individual infrasonic station. The RMS amplitude was calculated over 10 min windows with a 30 s overlap. (b) Relative spectrograms showing averaged spectral power over consecutive 10-min windows, with a 60 s Welch window and 50% overlap, expressed in dB re 1 Pa^2/Hz. The black dashed line points to the observed arrival time at ESLN station, and the gray ones are the arrival times of the second and third passages after having circumnavigated the Earth's atmosphere, hypothesized using the celerity of the observed first arrival time. (c) Raw infrasonic pressure signal recorded at ESLN, with the 2-min RMS amplitude superimposed in red. (d) The corresponding spectrogram calculated using 4096-sample (81.92 s) windows with 75% overlap. (e) Helicorder in the time interval 15 January 21:00 – 16 January 03:00.

Downloaded from pubs.geoscienceworld.org/ssa/srl/article-pdf/doi/10.1785/0220260189/8448745/srl-2026189.1.pdf by Universidad de Buenos Aires user on 27 November 2026

activity, with distinct bursts of acoustic-wave emission identified in the early infrasonic records (Matoza *et al.*, 2022; Podglajen *et al.*, 2022). Second, the nearly antipodal location of the recording station with respect to the source may result in the temporal proximity or overlap of arrivals associated with the two great-circle propagation paths, thereby contributing to the observed waveform complexity reported by Vergoz *et al.* (2022). Finally, different atmospheric propagation conditions and waveguides can further modify the arrival times and amplitudes of the infrasonic signals.

In particular, stratospheric winds strongly affect the propagation and ducting efficiency of infrasound, potentially leading to distinct arrivals with different travel times and amplitudes (Podglajen *et al.*, 2022; Vergoz *et al.*, 2022). Assuming a source time of 04:15 UTC and a source–receiver distance of 17,850 km, the observed arrivals are compatible with the celerities reported for long-range infrasonic propagation following the Hunga eruption (approximately 250–300 m/s). We tentatively interpret the first two arrivals (21:10, 22:55 UTC on 15 January 2022), as distinct infrasonic wave packets propagating along different atmospheric paths. The third (00:42 UTC on 16 January 2022) is also compatible with propagation along the longer great-circle (major-arc) path (Fig. 7a). However, differences in atmospheric propagation conditions and waveguide properties may also contribute to the observed arrival times and amplitudes.

Seismic signatures

The HTHH volcano eruption produced remarkably high-amplitude wideband 100–3300 s period atmospheric pressure waves that consisted of both elastically propagating infrasound and longer period acoustic gravity waves (Matoza *et al.*, 2022). As highlighted by recent works (e.g., Anthony *et al.*, 2022; Macpherson *et al.*, 2025; Scamfer *et al.*, 2026), these exceptional pressure perturbations have wavelengths of ∼10 to 30 km, and the resulting ground displacements provide a unique opportunity to examine acoustic-to-seismic coupling measurements that are sensitive to the material properties of the upper Earth's crust. In Italy, the seismic recordings produced by the atmospheric pressure wave generated by the Hunga eruption were recorded by all broadband seismic stations of the RSN network (Italian National Seismic Network, see Data and Resources), considering a time window starting from about 19:30 UTC on 15 January 2022. It is worth noting that no evidence of the pressure wave was detected by seismometers with an eigen period of ≤20 s, nor by the accelerometric sensors. Air-coupled Rayleigh waves generated by the atmospheric pressure wave hitting the ground were well observable on seismograms recorded by broadband seismometers characterized by flat responses at low frequency from 0.008 Hz (i.e., 120 s natural period) or at least 0.025 Hz (i.e., 40 s natural period), overall representing 85% of the broadband seismometers now operated by the RSN (Margheriti *et al.*, 2021).

Moreover, the RSN, also the recording provided by the Sos Enattos Mine (Sardinia Island, Italy) MN.SENA station belonging to the Mediterranean Very Broadband Seismic Network (MedNet, see Data and Resources), equipped with a 360 s Nanometrics Trillium 360GSN broadband seismometer, was considered. In general, concerning the remote stations installed in the Italian Alps or along the Apennines, ground-coupled pressure waves were clearly observable without any filtering, at least regarding the first phase on the horizontal components (e.g., MN.SENA, Fig. 8b); in particular, the very broadband station of MN.SENA installed in a very quiet remote site can clearly capture both the ground motion due to the M_w 5.7 (Matoza *et al.*, 2022) eruption (Fig. 8d) and the subsequent atmospheric pressure signal at frequencies down to 0.001 (Fig. 8b,d–f). On the contrary, in the case of seismic stations installed in urban areas characterized by high values of background ambient noise (e.g., IV.MILN, Fig. 8a,c), the application of a low-pass filter with a frequency threshold of 1 Hz was necessary.

Overall, all Italian RSN broadband stations showed the maximum energy content of the pressure wave in the frequency interval between 0.008 and 0.07 Hz, as recorded by many stations installed worldwide, for example, Anthony *et al.* (2022) and Macpherson *et al.* (2025).

In particular, Figure 8 shows the seismogram examples of ground-coupled atmospheric pressure waves recorded on the EW components (HHE) at stations IV.MILN (Fig. 8a,c), after low-pass filtering at MN.SENA (Fig. 8b,d). Figure 8a shows the first phase of the pressure wave recorded at IV.MILN station, equipped with a Nanometrics Trillium 40 s seismometer. The hypothetical arrival around 20:36 UTC was characterized by an emergent onset due to the high value of the background ambient noise of the site (Massa *et al.*, 2022) that, moreover, prevent to appreciate the further phases of the incoming pressure wave. Instead, the station MN.SENA installed in a remote site shows unfiltered raw data (Fig. 8b,d) characterized by a very good SNR considering a time window up to the 04:00 UTC of the 16 January 2022, allowing to clearly discriminate the subsequent phases of the recorded signal. Both at IV.MILN and MN.SENA (Fig. 8, bottom) the time–frequency analysis (Pinnegar, 2006) performed on the continuous data streams (HHE) confirms the evidence of the main phase recorded at IV.MILN with arrival around the 20:36 UTC and at MN.SENA three subsequent phases, approximately with arrivals observable at 21:50, 23:50 UTC of 15 January 2022, and at 01:30 UTC of 16 January 2022. In both cases, the recordings are due to a suite of pressure waves across an exceptionally broad spectrum of frequencies, including generally broadband infrasound (0.01–20 Hz) and the most relevant acoustic gravity Lamb wave (Lamb, 1881) able to generate long-period ($T \approx 100$ s) pressure variations that couple with the ground, primarily appearing as tilt-induced signals on the horizontal components of ground motion (Sorrells, 1971; Beauduin *et al.*, 1996).

Downloaded from pubs.geoscienceworld.org/ssa/srl/article-pdf/doi/10.1785/0220260189/8448745/srl-2026189.1.pdf by Universidad de Buenos Aires user on 27 November 2026

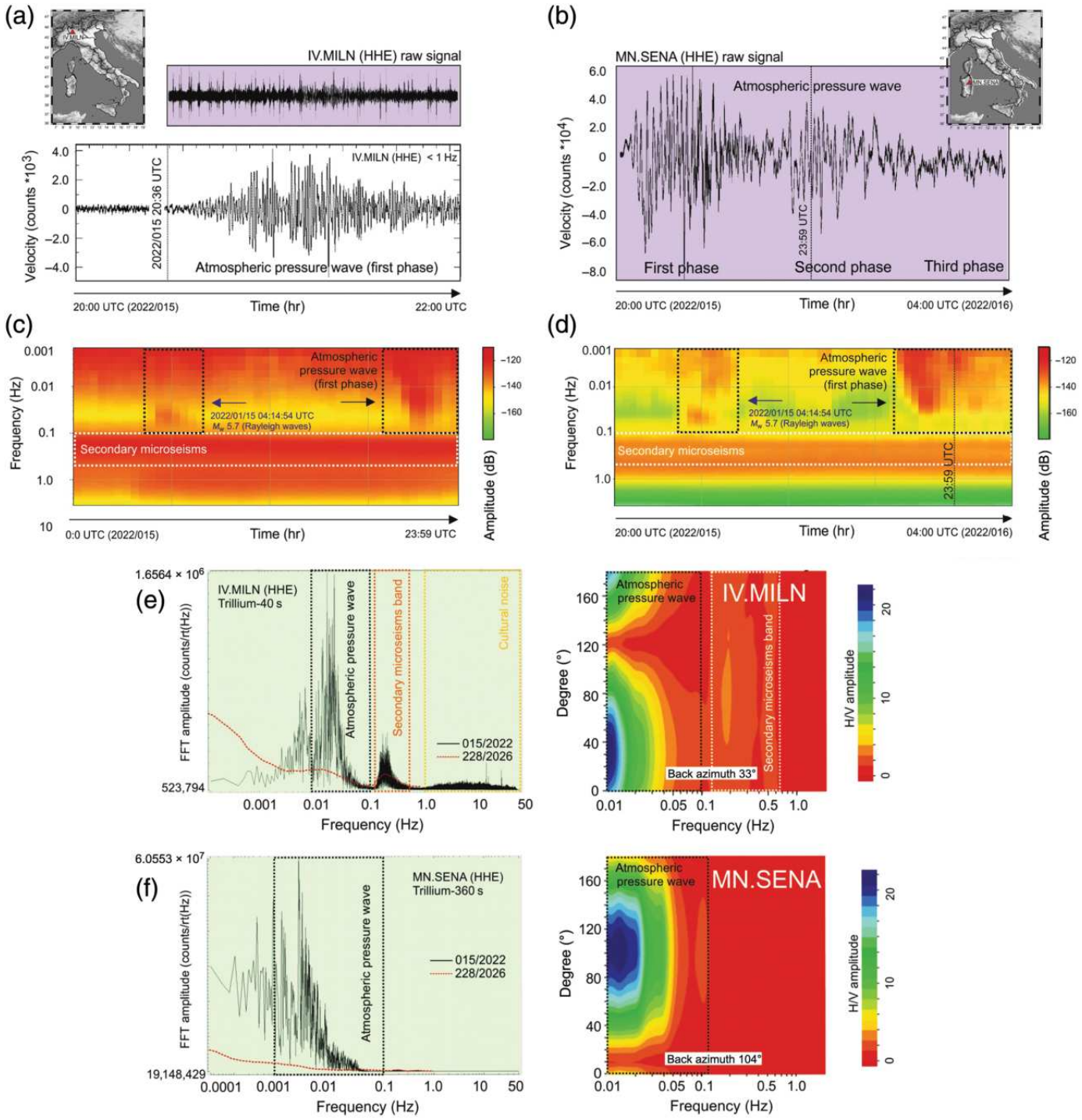

Figure 8. Examples of atmospheric pressure waves recorded on the east–west components (HHE) at (a) IV.MILN (Milan) station (inset in the top left corner), belonging to the RSN network (see Data and Resources), and (b) MN.SENA (North Sardinia) station (inset in the top right corner), belonging to the MedNet network (see Data and Resources). (c,d) For IV.MILN and MN.SENA, respectively, the time–frequency analysis (Pinnegar, 2006) was performed considering the continuous data streams filtered in the range 0.001–1.0 Hz. Fast Fourier spectra (left) and directional horizontal-to-vertical (H/V) spectral ratios (right) were calculated at (e) IV.MILN and (f) MN.SENA RSN stations, calculated considering 4 hr of recorded atmospheric pressure wave (first phase) filtered with a low-pass threshold at 1 Hz. In the left panels, the comparison between the daily spectra calculated on 15 January 2022 (black lines) and 16 August 2026 (red-dashed lines) is also shown. Directional HVSRs were computed using the Geopsy code (see Data and Resources).

Downloaded from pubs.geoscienceworld.org/ssa/srl/article-pdf/doi/10.1785/0220260189/8448745/srl-2026189.1.pdf by Universidad de Buenos Aires user on 27 November 2026

Figure 8e,f shows for the same target stations the Fourier spectra (left panels) and directional ambient noise horizontal-to-vertical spectral ratio (HVSR) (Nakamura, 1989) (right panels). The data processing for polarization included the application of an acausal four-poles Butterworth band-pass filter between 0.008 and 1 Hz, considering 1% cosine tapering at the limit of the selected windows. For each signal, the fast Fourier spectra (FFT) were computed considering subsequent sub-windows ranging from 240 to 540 s; subsequently, for computing directional spectral ratios, the north–south (NS) and EW components of ground motion were rotated between 0° and 175° by an angular step of 5, to compute 36 radial components. Finally, the spectra were smoothed using the (Konno and Ohmachi, 1998) window (b = 40) and then, for each considered angular step, the average HVSRs were computed considering the ratio between each rotated radial component and the vertical one. The results confirm at IV.MILN (Fig. 8e) a main energetic phase covering the frequency range 0.008–0.05 Hz with maximum energy between 0.009 and 0.02 Hz characterized by a marked polarization between 0° and 40° north. The results at IV.MILN show moreover the typical HVSR peak around 0.2 Hz due to the effects of the secondary microseismic band (Marzorati and Bindi, 2006) on the thick sedimentary cover that reaches around Milan depths of about 1.5 km (Massa *et al.*, 2022).

The same analysis performed at MN.SENA (Fig. 8f) confirms the arrival of subsequent phases as highlighted in Figure 8 characterized by frequency contents down to 0.0005 even if the main energetic contribution is observable in the range 0.005–0.05 Hz, in this case the incoming pressure wave from southeast shows clear polarization effects between 80° and 120° north (Fig. 8f).

Extending our consideration to the entire seismic network RSN (Fig. 9), almost all stations equipped with broadband 40 and 120 s seismometers allow us to observe the first phase of the pressure wave recorded in Italy in a time window spanning from 19:30 to 21:00 UTC. The station MN.SENA was the only station able to capture the three phases that well agree with the recording of the infrasonic station installed at Serra La Nave (ESLN, Fig. 7; see Data and Resources).

In this way, if the possible differences in the low-frequency part of the seismograms due to the different transfer functions of the broadband seismometer (Vergoz *et al.*, 2022) could be partially overcome by applying the deconvolution of the instrumental response, further biases reflect the large diversity of the site conditions of each station installed on hard rock, coastal areas, basins, and alluvial valleys (e.g., Macpherson *et al.*, 2025).

To analyze the capability of the RSN network to record the ground-coupled pressure wave, a spectral analysis in terms of FFT was performed considering the 160 six-channel RSN stations, as well as the MN.SENA stations, equipped with broadband 360 s seismometers. For each station, the FFT was calculated considering a frequency range of 0.008–0.1 Hz and a time window spanning from 19:30 to 00:00 UTC of 15 January 2022.

Then the integral of the spectral envelope was calculated to preliminarily approximate the energy content of each analyzed time window, considering both the vertical (HHZ) and the horizontal (HHN, HHE) ground-motion recordings. The results are reported in Figure 9a, where each circle is proportional to the integral of the spectra calculated in the selected frequency band that corresponds to the first phase of the recorded pressure wave. The results do not show any correlation between the observed energy content and some feature of the selected site: preliminary considerations concern an apparent decrease of the energy from north to south, probably due to the back azimuth of the pressure wavefront along the major arc (north-northeast [NNE] to NE), higher amplitude observed in correspondence with the urbanized areas (e.g., IV.MILN), at stations installed along the coast, in correspondence with heavy topography (e.g., IV.TEOL) or isolated cases along the Alps arc or in the Po alluvial basin. Overall, the horizontal components better capture the pressure wave, whereas the vertical ones always show lower amplitude. Considering the same RSN stations, a polarization analysis was performed considering just the first phase of the pressure wave to check the preferential direction of arrival and the direction of propagation at different sites. A particle motion analysis was performed on the horizontal components (Bormann *et al.*, 2013) together with the calculation of the rotated FFTs that allow calculating at each site the polarized HVSR, following the processing scheme previously described. In general, the directional HVSRs agree well in terms of incoming direction of propagation with the results obtained from the particle motion analyses, highlighting two different preferential directions of arrival, the first from north and the second from east, involving frequencies in the range 0.008–0.05 Hz. In this case, data show different incoming propagation, with prevalent NS (0°–50° N, Fig. 9b) and EW directions (80°–140° N, Fig. 9b). Concerning polarization effect a preliminary consideration is possible for the sites located in the center and at the edge of the Po plain, an alluvial basin in northern Italy with extension of about 50,000 km^2 and sediments with maximum depth of about 7 km (Pieri and Groppi, 1981; Bigi *et al.*, 1990). In this case at almost investigate sites (Fig. 9b), it was possible to observe a prevalent polarization of the frequency band with highest energy, around 0.01 Hz, in the NNE–south-southwest direction (i.e., 0°–40° N) that is the direction perpendicular to the main elongation of the target basin, leading to hypothesize a possible influence of the morphology of the area on the propagation of the pressure wave in the troposphere. It is worth finally mentioning the case of station IV.TEOL (Fig. 9b) located on a heavy and isolated topography bordering the Po basin, where the horizontal components show relevant amplitude and a marked polarization 120° N in a narrow range of frequency around 0.02 Hz,

Downloaded from pubs.geoscienceworld.org/ssa/srl/article-pdf/doi/10.1785/0220260189/8448745/srl-2026189.1.pdf by Universidad de Buenos Aires user on 27 November 2026

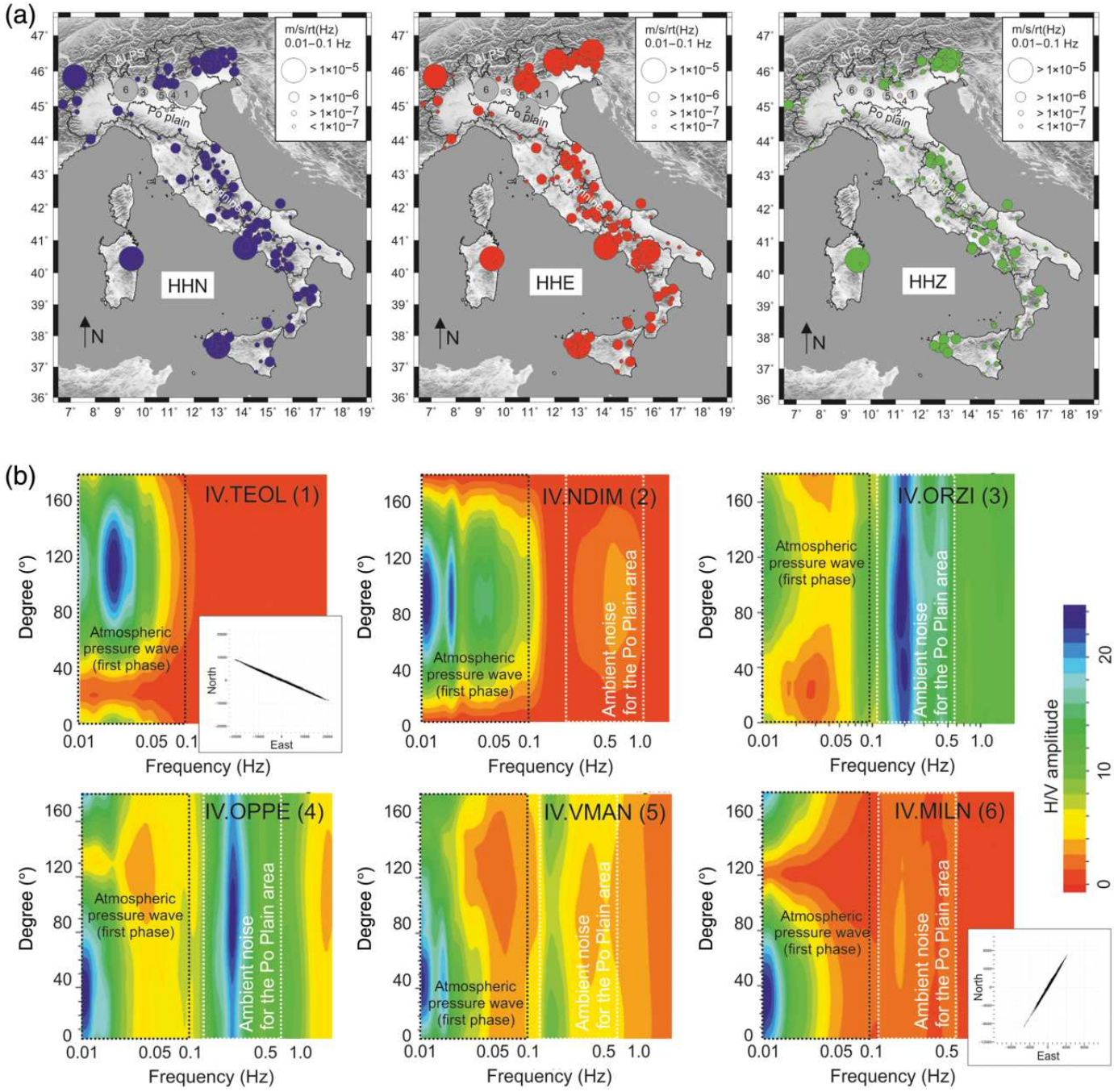

leading to no exclude also in this particular case a prevalent role of the morphology.

Ionospheric signatures

Once the dual-band GNSS data are gathered, one needs to retrieve the total electron content (TEC) along the ray path connecting the GNSS receiver and satellite. From wave propagation theory, it is known that free electrons are responsible for a range delay on GNSS observables that is proportional to the slant-path TEC (sTEC). Because of the nature of GNSS, the range delay is prone to errors of different natures; therefore, calibration is needed to obtain a reliable value of TEC. This

Figure 9. (a) Spectral analysis performed on the atmospheric pressure waves (first phase) recorded at 160 broadband RSN stations, filtered in the range 0.008–1.0 Hz. The circles in the maps are proportional to the energy content of each recording on the north–south (left, HHN), east–west (central, HHE), and vertical (right, HHZ) components, respectively. (b) Polarization analysis in terms of directional HVSRs calculated on selected RSN stations (gray symbols) installed in the Po plain and surrounding areas (Teolo, IV.TEOL; Novi di Modena, IV.NDIM; Orzinuovi, IV.ORZI, Oppeano, IV.OPPE, Volta Mantovana, IV.VMAN; and Milano, IV.MILN). Directional HVSRs were computed using the Geopsy code (see Data and Resources).

Downloaded from pubs.geoscienceworld.org/ssa/srl/article-pdf/doi/10.1785/0220260189/8448745/srl-2026189.1.pdf by Universidad de Buenos Aires user on 27 November 2026

is accomplished through the GG calibration technique (Ciraolo *et al.*, 2007), which assumes that each receiver-satellite couple's error is constant for brief periods of time (3 days). In addition to calculation biases, the calibration technique is in charge of projecting the sTEC to the vertical (vTEC), done by assuming a thin-shell ionosphere at 300 km altitude. An elevation cut-off mask of 20° is applied to avoid errors induced by multipath. To highlight wave features in the time evolution of vTEC, the time series needs to be detrended. To do so, we used the novel fast iterative filtering (FIF) technique Cicone (2020); Cicone and Zhou (2021) (see Data and Resources). FIF can be used to decompose non-stationary, nonlinear signals $s(t)$ into simple oscillatory components, which are called intrinsic mode functions (IMFs) according to the following equation:

$$s(t) = \sum_{i=1}^{N_{\mathrm{IMF}}} \mathrm{IMF}(t,v)_i + \mathrm{res}, \quad (1)$$

in which N_{IMF} is the total number of IMFs, with each having its own quasi-stationary frequency; res represents the decomposition residuals, which should be the non-oscillatory component, hence the background trend. Thanks to the IMFs having their own quasi-stationary frequency, it is possible to exploit FIF as a band-pass filter by summing, for each time step, the IMFs defined by an instantaneous frequency in the given band.

Thanks to previous studies, such as Themens *et al.* (2022) and Zhang *et al.* (2022), we know beforehand the expected traveling ionospheric disturbance (TID) period; hence, the frequency band given is 0.37–1.1 mHz (periods between 15 and 45 min). Once the wave features have been extracted for the whole RING network, the detrended TEC (dTEC) data are plotted on a travel-time distance plot (also referred to as a hodochrone) to better investigate HTHH-induced TID propagation. To increase the smoothness of the hodochrone, the data have been downsampled by averaging to a resolution of 90 s times 5 km.

Figure 10 shows the dTEC as a function of time and distance from HTHH, with the color representing the absolute value of dTEC in TEC units (TECu). The solid lines represent respectively the expected Lamb-wave propagation along the shorter and longer circle for a wave speed of 310 m/s. The dashed lines, instead represent the expected ionospheric waves, with their typical delay of around one hour with respect to the related neutral waves (Astafyeva, 2019). It can be noticed how many band-like features are present. Focusing on the parallel bands appearing after 19:30 UT, it is possible to note how they are almost parallel to the expected Lamb-wave propagation. This is a strong proof that the detected wave is a consequence of the upward propagation of secondary waves induced by the Lamb wave moving along the short circle toward the HTHH antipode, which is in northern Africa. If we look past 23:00 UT instead, we can notice how the TID looks like it propagates toward HTHH and shows a lower amplitude. This is again a strong proof since it is the Lamb wave that propagates along the long circle after it has gone beyond the epicenter antipode. Moreover, although the first wave appears slightly after the Lamb wave, the second one happens slightly in advance. This could be due to the geographical nature of the paths traveled by the two waves. Although the second one traveled mainly over the ocean surface, the first one passed through the whole of Eurasia, and it might have been slowed and weakened by mountain ranges and other geographical features.

The dTEC observations complement the conventional instrumentation by extending the multiparametric picture up to ionospheric heights. Their main added value is spatial: the dense, capillary distribution of GNSS receivers yields thousands of ionospheric piercing points, mapping the disturbance in space and time rather than at discrete stations, which let us track the Lamb-wave-induced secondary waves along both arcs and past the HTHH antipode (Fig. 10).

Discussion and Conclusion

The 15 January 2022 eruption of HTHH represented one of the most energetic volcanic events instrumentally recorded in recent decades and provided an exceptional opportunity to investigate the coupling between the solid Earth, atmosphere, and ionosphere on a planetary scale. The multiparameter observations collected by INGV networks in Italy demonstrate that even geophysical monitoring systems installed thousands of kilometers from the source are capable of detecting and characterizing the propagation of atmospheric and seismic perturbations generated by extreme volcanic explosions.

The combination of seismic, barometric, infrasound, strain meter, and GNSS observations allowed us to reconstruct the arrival and propagation of Lamb waves traveling along both the minor and major arcs around the globe. The observed propagation velocity of approximately 310 m/s is fully consistent with previous global studies (Matoza *et al.*, 2022; Vergoz *et al.*, 2022; Yuen *et al.*, 2022) and confirms the extraordinary coherence of the atmospheric disturbance generated by the eruption. The repeated passages of the pressure wave, recorded several times after circumnavigating the Earth, emphasize the remarkable energy released by the HTHH event.

The infrasonic signals associated with the HTHH eruption were clearly detected at several stations around Mt. Etna and exhibited multiple arrivals, including two distinct wave packets on 15 January 2022, characterized by different apparent propagation velocities. This variability, together with the complex temporal structure of the signals, may reflect the combined influence of the multipulse source and the atmospheric propagation conditions along different paths, as previously reported for the HTHH infrasonic observations (Matoza *et al.*, 2022; Podglajen *et al.*, 2022; Vergoz *et al.*, 2022). Such observations highlight the potential of long-range infrasonic signals to provide independent constraints on atmospheric propagation conditions and waveguide characteristics.

Downloaded from pubs.geoscienceworld.org/ssa/srl/article-pdf/doi/10.1785/0220260189/8448745/srl-2026189.1.pdf by Universidad de Buenos Aires user on 27 November 2026

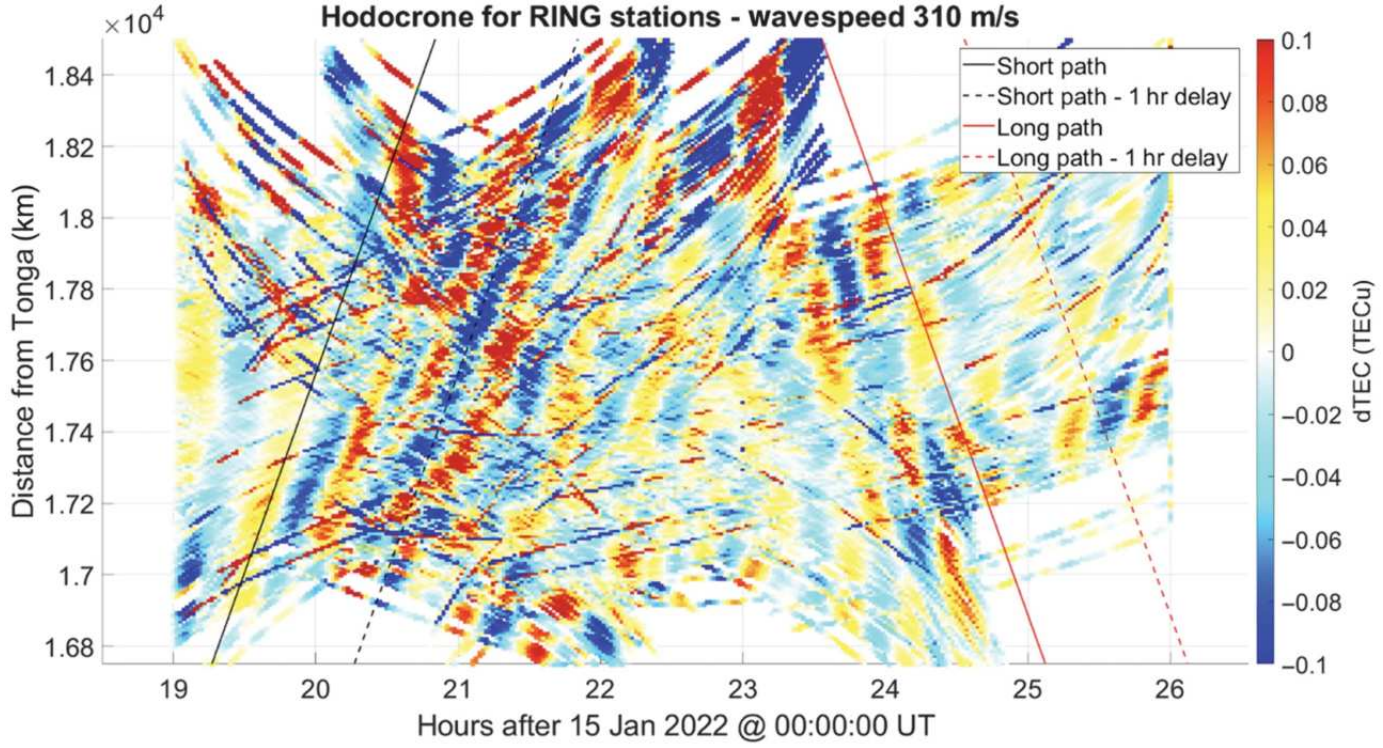

Figure 10. Hodochrone showing detrended total electron content (dTEC) in the distance range 16,500–18,500 km from HTHH as a function of UT. The black and red solid lines represent the lamb-wave propagation, and the dashed ones are related to the ionospheric wave.

The global propagation of ultra-long-period acoustic-gravity and Lamb waves generated by the 15 January 2022 HTHH eruption provided an unprecedented opportunity to examine air-to-ground acoustic-seismic coupling across regional broadband seismic networks. Although atmospheric pressure variations recorded on horizontal channels have traditionally been treated as long-period seismic noise (Sorrells, 1971; Beauduin *et al.*, 1996), recent studies demonstrate that high-amplitude, wide-band infrasonic sources act as an extraordinary probe for solid Earth elasticity. In particular, Anthony *et al.* (2022) and Macpherson *et al.* (2025) showed that the low-frequency acoustic energy (< 0.05 Hz) from the Hunga eruption excited the solid Earth to unprecedented penetration depths, effectively probing upper-crustal elastic properties down to 5 km. This deeply penetrating coupling contrasts sharply with routine wind- or local explosion-induced air-to-ground coupled waves (AGCWs), which are typically constrained to the uppermost incoherent layers or shallowest tens of meters (Tanimoto and Wang, 2019).

AGCWs can provide insight into both the acoustic source and the subsurface, but interpretation can be challenging because the observed ground motions are highly sensitive to subsurface structure. Characteristics of the seismic particle motion are particularly important: they are used to identify AGCWs and to inform methods that estimate the back azimuth of the incident infrasound wave (Langston, 2004; Bishop *et al.*, 2023).

In the context of the Italian National Seismic Network (RSN) managed by INGV, the passage of the HTHH atmospheric pressure wave excited broadband seismometers located across different geological and morphological domains. A critical manifestation of this phenomenon is observed in the Po Plain in Figure 10, a deep sedimentary basin characterized by pronounced long-period seismic site amplifications (e.g., Luzi *et al.*, 2013; Massa and Augliera, 2013; Mascandola *et al.*, 2019; Lai *et al.*, 2020). The incident atmospheric pressure wave exerted a transient surface loading that induced measurable ground motion across the basin. Applying the directional HVSR technique to these low-frequency air-coupled signals allows us to bypass traditional ambient microseism limitations and image impedance contrasts at exceptional depths. Rather than reflecting local topographical tilt or shallow soil compliance, the low-frequency HVSR response in the Po Plain marks the primary acoustic-seismic energy transfer across deep-seated structural boundaries, outlining possible impedance contrasts between overlying sedimentary covers of increasing density and the underlying competent basement, also considering that likely more rigid material is more resistant to coupling, while shallower, seismically slower material is more readily excited by the pressure waves (Sorrells, 1971). Furthermore, the observational framework established by Scamfer *et al.* (2026) provides further possible diagnostic criteria for interpreting such basin-scale responses. Although classical elasticity models (Sorrells, 1971; Ben-Menahem and Singh, 1981) predict generally retrograde particle motion for AGCWs, empirical observations reveal that prograde motion

Downloaded from pubs.geoscienceworld.org/ssa/srl/article-pdf/doi/10.1785/0220260189/8448745/srl-2026189.1.pdf by Universidad de Buenos Aires user on 27 November 2026

dominates in low-velocity environments (such as sedimentary embayments, Scamfer *et al.*, 2026) where the apparent acoustic wave speed exceeds the local shear-wave velocity of the ground. The strong impedance contrasts and vertical density gradients within the Po Plain sediment fill naturally promote complex particle motion behaviors, including frequency-dependent shifts from prograde to retrograde motion, as the effective sampling depth transitions from shallow unconsolidated strata to deeper, more rigid formations. Consequently, analyzing the multiparametric response of the INGV broadband network to the Hunga event not only documents a rare atmospheric–lithospheric coupling event, but also demonstrates the efficacy of ultra-long-period atmospheric pressure waves for deep crustal profiling and basin-amplification characterization in Italy.

Our results highlight the importance of integrated multiparametric monitoring systems and real-time sources and platforms for the observation of complex geophysical phenomena. In particular, the simultaneous detection of pressure perturbations by barometers, strain-induced deformation by borehole dilatometers, ground-coupled air waves by broadband seismic stations, and ionospheric disturbances by GNSS receivers demonstrates the strong coupling between atmosphere and lithosphere across multiple spatial and temporal scales.

The Italian monitoring infrastructure also proved capable of providing valuable regional case studies of long-range atmospheric wave propagation. Dense regional networks installed at Etna, Stromboli, Phlegraean Fields, and northern Italy allowed detailed analyses of arrival times, wave amplitudes, frequency content, and propagation directions. These observations suggest that local geological and morphological conditions may influence the propagation and polarization of ground-coupled atmospheric waves, particularly in sedimentary basins such as the Po Plain.

The ionospheric observations further confirm that the atmospheric perturbations generated by the eruption propagated upward through the atmosphere and induced TIDs detectable over the Mediterranean region. The good agreement between expected Lamb-wave propagation times and the observed TEC perturbations demonstrates the effectiveness of GNSS networks for investigating lithosphere–atmosphere–ionosphere coupling processes associated with major volcanic eruptions.

In the present case, the value of TEC for early warning is demonstrative rather than operational: Italy lies in the far field, so the ionospheric signatures arrived hours after the eruption with no local lead time. The event nonetheless shows that the RING GNSS network reliably detected the Lamb-wave-induced perturbations of an extreme, distant source within the same real-time infrastructure used for seismic and barometric monitoring. This confirms that TEC can be produced and interpreted operationally alongside conventional parameters, supporting its use for closer, tsunamigenic sources as a complementary, globally distributed observable within a multiparametric early warning framework.

From an operational perspective, this study also underlines the growing relevance of multiparametric networks for early warning applications. The capability of distributed real-time monitoring systems to rapidly identify anomalous atmospheric and geophysical signals can contribute to the development of integrated warning strategies for volcanic eruptions, tsunamis, and other natural hazards. Equally important is the role of rapid science communication and delivery to decision-makers, particularly during globally relevant crises where timely interpretation of observational data is essential for civil protection agencies and scientific institutions.

The HTHH eruption demonstrated that modern monitoring infrastructures can act as globally distributed observatories capable of recording extreme geophysical phenomena far beyond national boundaries. Future developments should therefore focus on strengthening interoperability among international monitoring systems, improving real-time data exchange, and integrating atmospheric, seismic, and ionospheric observations into unified operational frameworks.

Finally, the exceptional dataset generated by the HTHH eruption represents a benchmark for future studies investigating atmospheric wave propagation, seismoacoustic coupling, and ionospheric responses to major volcanic eruptions. The challenge of this contribution lies in coordinating and analyzing the various datasets, recorded by many different monitoring realities, and demonstrating that the INGV has significant operational potential that has never been utilized to date. The Hunga event was chosen to highlight this operational effectiveness. One of the lessons learned is that in 2023 INGV started to extend some selected stations of the national seismic network by infrasound sensors. Once processing times are reduced to (quasi-) real time, the data analysis products may potentially provide in the future a contribution to early warning and emergency response.

Data and Resources

Information about the Italian National Seismic Network (RSN-INGV) are available at doi: 10.13127/SD/X0FXnH7QfY, and information about the Mediterranean Very Broadband Seismographic Network is available at doi: 10.13127/SD/fBBBtDtd6q and https://eida.ingv.it/it/network/MN. The webpage of the European Integrated Data Archive is available at http://www.orfeus-eu.org/data/eida/. The website of the International Federation of Digital Seismograph Networks is available at https://www.fdsn.org/. The SEED-channels description is available at the website of the Southern California Earthquake Data Center, https://scedc.caltech.edu/data/station/seed.html. Information about all Istituto Nazionale di Geofisica e Vulcanologia stations cited in the text is available at https://terremoti.ingv.it/en/instruments/network/IV. Details about the infrasonic station installed at Serra La Nave are available at https://ingvvulcani.com/2022/01/18/il-boato-che-ha-fatto-il-giro-del-mondo/. Information about the dynamic planet multiparameter northern Italy seismic network are available at http://terremoti.ingv.it/instruments/network/ZO. Infrasound data are available at Sciotto *et al.* (2022). The fast iterative filtering software is available at http://www.cicone.com,

Downloaded from pubs.geoscienceworld.org/ssa/srl/article-pdf/doi/10.1785/0220260189/8448745/srl-2026189.1.pdf by Universidad de Buenos Aires user on 27 November 2026

https://github.com/Acicone/FIF, and https://it.mathworks.com/matlabcentral/fileexchange/69525-fif. Korea's GeoKompsat weather satellite is available at https://cimss.ssec.wisc.edu/satellite-blog/archives/43894. The Rete Integrata Nazionale RING is available at https://webring.gm.ingv.it/. The origin time of the associated seismic events is available at https://earthquake.usgs.gov/earthquakes/eventpage/pt22015050/executive. The data to RSN network by the Italian National Seismic Network are available at https://eida.ingv.it/it/network/IV. The data from Incorporated Research Institutions for Seismology Data Management System are available at https://ds.iris.edu/ds/nodes/dmc/. All websites were last accessed in November 2026.

Declaration of Competing Interests

The authors acknowledge that there are no conflicts of interest recorded.

Acknowledgments

The authors thank Fabio Varchetta (INGV-Milan) for his contribution, especially during the revision phases of the manuscript. The authors are grateful to 1. LgT. D. Palella e Ten. Col. A. Celozzi of Stato Maggiore Aeronautica Ufficio Generale Aviazione Militare e Meteorologia for making available the meteo data shown in Figure 3. The authors also thank Editor-in-Chief Allison Bent, Guest Editor, and the reviewers Adam Ringler and David Fee for their comments, which helped to improve clarity and quality of this article.

References

Anthony, R. E., A. T. Ringler, T. Tanimoto, R. S. Matoza, S. De Angelis, and D. C. Wilson (2022). Earth's upper crust seismically excited by infrasound from the 2022 Hunga Tonga–Hunga Ha'apai eruption, Tonga, *Seismol. Res. Lett.* **94,** no. 2A, 603–616, doi: 10.1785/0220220252.

Astafyeva, E. (2019). Ionospheric detection of natural hazards, *Rev. Geophys.* **57,** 1265–1288, doi: 10.1029/2019RG000668.

Baker, E., G. Massoth, C. DeRonde, J. Lupton, and B. McInnes (2002). Observations and sampling of an ongoing subsurface eruption of Kavachi volcano, Solomon Islands, May 2000, *Geology* **30,** no. 11, 975–978.

Beauduin, R., P. Lognonné, J. P. Montagner, S. Cacho, J. F. Karczewski, and M. Morand (1996). *Bull. Seismol. Soc. Am.* **86,** no. 6, 1760–1769. doi: 10.1785/BSSA0860061760.

Ben-Menahem, A., and S. J. Singh (1981). *Seismic Waves and Sources*, Springer, New York, 1129 pp.

Bigi, G., D. Costantino, M. Parotto, R. Sartori, and P. Scandone (1990). Structural model of Italy scala 1: 500.000-Consiglio Nazionale delle Ricerche progetto Finalizzato Geodinamica, *Tech. Rep.*, Società Elaborazioni Cartografiche (S.E.L.CA.), Firenze, 9 fogli.

Bishop, J. W., M. M. Haney, D. Fee, R. S. Matoza, K. F. McKee, and J. J. Lyons (2023). Back-Azimuth estimation of air-to-ground coupled infrasound from transverse coherence minimization, *Seism. Record* **3,** no. 4, 249–258. doi: 10.1785/0320230023.

Bormann, P., S. Wendt, and D. Di Giacomo (2013). Seismic sources and source parameters, in *New Manual of Seismological Observatory Practice 2 (NMSOP-2)*, P. E. Bormann (Editor), Deutsches GeoForschungs Zentrum GFZ, Potsdam, 1–259, doi: 10.2312/GFZ.NMSOP-2_ch3.

Carracedo, J., F. Pérez-Torrado, A. Rodríguez-González, J. L. Fernández-Turiel, A. Klügel, V. R. Troll, and S. Wiesmaier (2012). The ongoing volcanic eruption of El Hierro, Canary Islands, *Eos Trans. AGU* **93**, 89–90.

Cicone, A. (2020). Iterative filtering as a direct method for the decomposition of non stationary signals, *Numer. Algor.* **85,** 811–827, doi: 10.1007/s11075-019-00838-z.

Cicone, A., and H. Zhou (2021). Numerical analysis for iterative filtering with new efficient implementations based on FFT, *Numer. Math.* **147,** 1–28, doi: 10.1007/s00211-020-01165-5.

Ciraolo, L., F. Azpilicueta, C. Brunini, A. Meza, and S. M. Radicella (2007). Calibration errors on experimental slant total electron content (TEC) determined with GPS, *J. Geodynam.* **81,** 111–120, doi: 10.1007/s00190-006-0093-1.

De Ronde, C. E. J., E. T. Baker, G. J. Massoth, J. E. Lupton, I. C. Wright, R. J. Sparks, S. C. Bannister, M. E. Reyners, S. L. Walker, *et al.* (2007). Submarine hydrothermal activity along the mid-Kermadec Arc, New Zealand: Large-scale effects on venting, *Geochem. Geophys. Geosys.* **8,** Q07007.

Ferrari, E., M. Massa, S. Lovati, F. Di Michele, and A. Rizzo (2024). Multiparametric stations for real-time monitoring and long-term assessment of natural hazards, *Front. Earth Sci.* **12,** doi: 10.3389/feart.2024.1412900.

Fiske, R. S., K. V. Cashman, A. Shibata, and K. Watanabe (1998). Tephra dispersal from Myojinsho, Japan, during its shallow submarine eruption of 1952–1953, *Bull. Volcanol.* **59,** 262–275.

Garvin, J. (2022). Dramatic changes at Hunga Tonga-Hunga Ha'apai, available at https://science.nasa.gov/earth/earth-observatory/dramatic-changes-at-hunga-tonga-hunga-haapai-149367/ (last accessed May 2026).

INGV (2006). Rete sismica nazionale (RSN) Italy, *Istituto Nazionale di Geofisica e Vulcanologia (INGV)*, doi: 10.13127/SD/X0FXNH7QFY.

Kennett, B., E. Engdahl, and R. Buland (1995). Constraints on seismic velocities in the earth from travel times, *Geophys. J. Int.* **122**, 108–124.

Konno, K., and T. Ohmachi (1998). Ground-motion characteristics estimated from spectral ratio between horizontal and vertical components of microtremor, *Bull. Seismol. Soc. Am.* **88,** no. 1, 228–241, doi: 10.1785/BSSA0880010228.

Kraft, T., O. K. A. Ling, T. Toledo, B. Scheu, S. C. Stähler, J. Clinton, and S. Stange (2023). An antipodal seismic and (infra)acoustic view from central Europe on the 15 January 2022 Hunga-Tonga-Hunga-Ha'apai eruption, *Seismol. Res. Lett.* **94,** no. 3, 1318–1333, doi: 10.1785/0220220254.

Lai, C. G., V. Poggi, A. Famà, E. Zuccolo, F. Bozzoni, C. Meisina, R. Bonì, L. Martelli, M. Massa, C. Mascandola, *et al.* (2020). An interdisciplinary and multi-scale approach to assess the spatial variability of ground motion for seismic microzonation: The case study of Cavezzo municipality in Northern Italy, *Eng. Geol.* **274,** 105722, doi: 10.1016/j.enggeo.2020.105722.

Lamb, H. (1881). On the vibrations of an elastic sphere, *Proc. London Math. Soc.* **13,** no. 1, 189–212, doi: 10.1112/plms/s1-13.1.189.

Langston, C. A. (2004). Seismic ground motions from a bolide shock wave, *J. Geophys. Res. Solid Earth* **109,** no. B12, doi: 10.1029/2004JB003167.

Luzi, L., F. Pacor, G. Ameri, R. Puglia, P. Burrato, M. Massa, P. Augliera, G. Franceschina, S. Lovati, and R. Castro (2013).

Downloaded from pubs.geoscienceworld.org/ssa/srl/article-pdf/doi/10.1785/0220260189/8448745/srl-2026189.1.pdf by Universidad de Buenos Aires user on 27 November 2026

Overview on the strong-motion data recorded during the May-June 2012 Emilia seismic sequence, *Seismol. Res. Lett.* **84,** no. 4, 629–644, doi: 10.1785/0220120154.

Luzi, L., R. Puglia, E. Russo, M. D'Amico, C. Felicetta, F. Pacor, G. Lanzano, U. Çeken, J. Clinton, *et al.* (2016). The European strong-motion database: A platform to access accelerometric data, *Seismol. Res. Lett.* **87,** no. 4, doi: 10.1785/0220150278.

Macpherson, K., D. Fee, S. Awender, B. Chow, J. Colwell, S. Delamere, and M. Haney (2025). Alaska upper crustal velocities revealed by air-to-ground coupled waves from the 2022 Hunga Tonga-Hunga Ha'apai eruption, *Seismica* **4,** no. 2, doi: 10.26443/seismica.v4i2.1557.

Madonia, P., A. Bonaccorso, A. Bonforte, C. Buonocunto, A. Cannata, L. Carleo, C. Cesaroni, G. Currenti, S. De Gregorio, B. Di Lieto, *et al.* (2023). Propagation of perturbations in the lower and upper atmosphere over the Central Mediterranean, driven by the 15 January 2022 Hunga Tonga-Hunga Ha'apai volcano explosion, *Atmosphere* **14,** no. 1, doi: 10.3390/atmos14010065.

Margheriti, L., C. Nostro, O. Cocina, M. Castellano, M. Moretti, V. Lauciani, M. Quintiliani, A. Bono, F. M. Mele, S. Pintore, *et al.* (2021). Seismic surveillance and earthquake monitoring in Italy, *Seismol. Res. Lett.* **92,** no. 3, 1659–1671, doi: 10.1785/0220200380.

Marzorati, S., and D. Bindi (2006). Ambient noise levels in north central Italy, *Geochem. Geophys. Geosys.* **7,** no. 9, doi: 10.1029/2006GC001256.

Mascandola, C., M. Massa, S. Barani, D. Albarello, S. Lovati, L. Martelli, and V. Poggi (2019). Mapping the seismic bedrock of the Po Plain (Italy) through ambient-vibration monitoring, *Bull. Seismol. Soc. Am.* **109,** no. 1, 164–177, doi: 10.1785/0120180193.

Massa, M., and P. Augliera (2013). Teleseisms as estimators of experimental longperiod site amplification: Application to the po plain (Italy) for the 2011 Mw 9.0 Tohoku-Oki (Japan) earthquake, *Bull. Seismol. Soc. Am.* **103,** no. 5, 2541–2556, doi: 10.1785/0120120164.

Massa, M., S. Lovati, G. Franceschina, E. D'Alema, S. Marzorati, S. Mazza, M. Cattaneo, G. Selvaggi, A. Amato, A. Michelini, *et al.* (2014). ISMD, a web portal for real-time processing and dissemination of INGV strong-motion data, *Seismol. Res. Lett.* **85,** no. 4, 863–877, doi: 10.1785/0220140024.

Massa, M., S. Lovati, R. Puglia, G. Brunelli, A. Lorenzetti, C. Mascandola, C. Felicetta, F. Pacor, and L. Luzi (2022). Seismostratigraphic model for the urban area of Milan (Italy) by ambient-vibration monitoring and implications for seismic site effects assessment, *Front. Earth Sci.* **10,** doi: 10.3389/feart.2022.915083.

Massa, M., A. L. Rizzo, A. Lorenzetti, S. Lovati, E. D'Alema, R. Puglia, S. Carannante, A. Piersanti, G. Galli, and V. Cannelli, *et al.* (2021). La rete del lago di Garda: una nuova infrastruttura dell'INGV per il monitoraggio multiparametrico, available at https://ingvterremoti.com/2021/12/10/la-rete-del-lago-di-garda-una-nuova-infrastruttura-dellingv-per-il-monitoraggio-multiparametrico/ (last accessed May 2026) (in Italian).

Matoza, R. S., D. Fee, J. D. Assink, A. M. Iezzi, D. N. Green, K. Kim, L. Toney, T. Lecocq, S. Krishnamoorthy, J. M. Lalande, *et al.* (2022). Atmospheric waves and global seismoacoustic observations of the January 2022 Hunga eruption, Tonga, *Science* **377,** no. 6601, 95–100, doi: 10.1126/science.abo7063.

Michelini, A., L. Margheriti, M. Cattaneo, G. Cecere, G. D'Anna, A. Delladio, M. Moretti, S. Pintore, A. Amato, A. Basili, *et al.* (2016). The Italian National Seismic Network and the earthquake and tsunami monitoring and surveillance systems, *Adv. Geosci.* **43,** 31–38, doi: 10.5194/adgeo-43-31-2016.

Nakamura, Y. (1989). A method for dynamic characteristics estimation of subsurface using microtremor on the ground surface, *Quarterly Report of Railway Technical Research 30*, 25–33.

Perttu, A., C. Caudron, J. D. Assink, D. Metz, D. Tailpied, B. Perttu, C. Hibert, D. Nurfiani, C. Pilger, M. Muzli, *et al.* (2020). Reconstruction of the 2018 tsunamigenic flank collapse and eruptive activity at Anak Krakatau based on eyewitness reports, seismo-acoustic and satellite observations, *Earth Planet. Sci. Lett.* **541,** 116268, doi: 10.1016/j.epsl.2020.116268.

Pieri, M., and G. Groppi (1981). Subsurface geological structure of the Po Plain, Italy, in *Progetto finalizzato geodinamica/sottoprogetto "modello strutturale"*, C.N.R. Publishing.

Pinnegar, C. R. (2006). Polarization analysis and polarization filtering of three-component signals with the time-frequency S transform, *Geophys. J. Int.* **165,** no. 2, 596–606, doi: 10.1111/j.1365-246X.2006.02937.x.

Podglajen, A., A. Le Pichon, R. F. Garcia, S. Gérier, C. Millet, K. Bedka, K. Khlopenkov, S. Khaykin, and A. Hertzog (2022). Stratospheric balloon observations of infrasound waves from the 15 January 2022 Hunga eruption, Tonga, *Geophys. Res. Lett.* **49,** no. 19, e2022GL100833, doi: 10.1029/2022GL100833.

Pondrelli, S., F. Di Luccio, L. Scognamiglio, I. Molinari, S. Salimbeni, A. D'Alessandro, and P. Danecek (2019). The first very broadband Mediterranean network: 30 yr of data and seismological, *Seismol. Res. Lett.* **91,** no. 2A, 787–802, doi: 10.1785/0220190195.

Proud, S. R., A. T. Prata, and S. Schmauss (2022). The January 2022 eruption of Hunga tonga-hunga ha'apai volcano reached the mesosphere, *Science* **378,** 554–557. doi: 10.1126/science.abo4076.

Purkis, S. J., S. N. Ward, N. M. Fitzpatrick, J. B. Garvin, D. Slayback, S. J. Cronin, M. Palaseanu-Lovejoy, and A. Dempsey (2023). The 2022 hunga-tonga megatsunami: Near-field simulation of a once-in-a-century event, *Sci. Adv.* **9,** no. 15, eadf5493, doi: 10.1126/sciadv.adf5493.

Scamfer, L., D. Fee, J. Bishop, M. Haney, and K. Macpherson (2026). The influence of shallow subsurface properties on particle motion in acoustic-seismic coupling, *Seismica* **5,** no. 1, doi: 10.26443/seismica.v5i1.2254.

Sciotto, M., L. Scuderi, O. Torrisi, C. Cassisi, and E. Privitera (2022). Infrasonic signals recorded at Mt. Etna stations during period 15–19 January 2022 (ISGN) (Versione 1) [Data], doi: 10.13127/etna_infra/raw_20220115_19.

Smith, I. E. M., and R. C. Price (2006). The Tonga-Kermadec arc and Havre-Lau back-arc system: their role in the development of tectonic and magmatic models for the western Pacific, *J. Volcanol. Geotherm. Res.* **156,** 315–331, doi: 10.1016/j.jvolgeores.2006.03.006.

Sorrells, G. G. (1971). A preliminary investigation into the relationship between long-period seismic noise and local fluctuations in the atmospheric pressure field, *Geophys. J. Roy. Astron. Soc.* **26,** nos. 1/4, 71–82, doi: 10.1111/j.1365-246X.1971.tb03383.x.

Taha, G., R. Loughman, P. R. Colarco, T. Zhu, L. W. Thomason, and G. Jaross (2022). Tracking the 2022 Hunga Tonga-Hunga Ha'apai aerosol cloud in the upper and middle stratosphere using space-based observations, *Geophys. Res. Lett.* **49,** no. 23, doi: 10.1029/2022GL100091.

Downloaded from pubs.geoscienceworld.org/ssa/srl/article-pdf/doi/10.1785/0220260189/8448745/srl-2026189.1.pdf by Universidad de Buenos Aires user on 27 November 2026

Tanimoto, T., and J. Wang (2019). Theory for deriving shallow elasticity structure from colocated seismic and pressure data, *J. Geophys. Res. Solid Earth* **124,** no. 6, 5811–5835, doi: 10.1029/2018JB017132.

Themens, D. R., C. Watson, N. Žagar, S. Vasylkevych, S. Elvidge, A. McCaffrey, P. Prikryl, B. Reid, A. Wood, and P. T. Jayachandran (2022). Global propagation of ionospheric disturbances associated with the 2022 Tonga volcanic eruption, *Geophys. Res. Lett.* **49,** no. 7, doi: 10.1029/2022GL098158.

Van Eaton, A. R., J. Lapierre, S. A. Behnke, C. Vagasky, C. J. Schultz, M. Pavolonis, K. Bedka, and K. Khlopenkov (2023). Lightning rings and gravity waves: Insights into the giant eruption plume from Tonga's Hunga volcano on 15 January 2022, *Geophys. Res. Lett.* **50,** 10, doi: 10.1029/2022GL102341.

Vaughan, R., and P. Webley (2010). Satellite observations of a surtseyan eruption: Hunga Ha'apai, Tonga, *J. Volcanol. Geotherm. Res.* **198,** 177–186.

Venzke, E. (2022). Global volcanism program, 2022. Report on Hunga Tonga-Hunga Ha'apai (Tonga), *Bulletin of the Global Volcanism Network*, Vol. 47, Smithsonian Institution, available at https://volcano.si.edu/volcano.cfm?vn=243040 (last accessed November 2026).

Vergoz, J., P. Hupe, C. Listowski, A. Le Pichon, M. A. Garcés, E. Marchetti, P. Labazuy, L. Ceranna, C. Pilger, P. Gaebler, *et al.* (2022). IMS observations of infrasound and acoustic-gravity waves produced by the January 2022 volcanic eruption of Hunga, Tonga: A global analysis, *Earth Planet. Sci. Lett.* **591,** 117639. doi: 10.1016/j.epsl.2022.117639.

Yuen, D. A., M. A. Scruggs, F. J. Spera, Y. Zheng, H. Hu, S. R. McNutt, G. Thompson, K. Mandli, B. R. Keller, S. S. Wei, *et al.* (2022). Under the surface: Pressure-induced planetary-scale waves, volcanic lightning, and gaseous clouds caused by the submarine eruption of Hunga Tonga-Hunga Ha'apai volcano, *Earthq. Res. Adv.* doi: 10.1016/j.eqrea.2022.100134.

Zhang, S. R., J. Vierinen, E. Aa, L. P. Goncharenko, P. J. Erickson, W. Rideout, A. J. Coster, and A. Spicher (2022). 2022 Tonga volcanic eruption induced global propagation of ionospheric disturbances via lamb waves, *Front. Astron. Space Sci.* **9,** doi: 10.3389/fspas.2022.871275.

Manuscript received 18 May 2026
Published online 25 November 2026

Downloaded from pubs.geoscienceworld.org/ssa/srl/article-pdf/doi/10.1785/0220260189/8448745/srl-2026189.1.pdf by Universidad de Buenos Aires user on 27 November 2026